Effects of composition, crystal structure, and surface orientation on band alignment of divalent metal oxides: A first-principles study

Yoyo Hinuma,[1,2,*] Yu Kumagai,[3] Isao Tanaka,[4,2] and Fumiyasu Oba[5,2,†]

[1]*Center for Frontier Science, Chiba University, Chiba 263-8522, Japan*

[2]*Center for Materials Research by Information Integration, Research and Services Division of Materials Data and Integrated System, National Institute for Materials Science, Tsukuba 305-0047, Japan*

[3]*Materials Research Center for Element Strategy, Tokyo Institute of Technology, Yokohama 226-8503, Japan*

[4]*Department of Materials Science and Engineering, Kyoto University, Kyoto 606-8501, Japan*

[5]*Laboratory for Materials and Structures, Institute of Innovative Research, Tokyo Institute of Technology, Yokohama 226-8503, Japan*

(Received 27 September 2018; published 10 December 2018)

Using first-principles calculations, this paper systematically investigates the ionization potentials (IPs) and electron affinities (EAs) of nonpolar surfaces of binary divalent metal oxides with formally closed-shell electronic structures, namely, BeO, MgO, CaO, SrO, BaO, ZnO, HgO, SnO, and PbO in relevant crystal structures. An emphasis is put on the understanding of the effects of chemical composition, crystal structure, and surface orientation on the surface band positions. Slab models for nonpolar surfaces are automatically generated using a proposed algorithm that provides a set of unique nonpolar surface orientations. A non-self-consistent dielectric-dependent hybrid functional approach is employed that is shown to provide a significant improvement in the band-gap, IP, and EA evaluation over standard density functional theory calculations using the generalized gradient approximation. The valence band maximum, O 2*s* band center, and O-site local potential versus the vacuum level are examined for prototypical rocksalt, wurtzite, and zincblende surfaces of selected systems without atomic relaxation. All of these quantities are found to qualitatively follow the tendency in the Madelung potential at the O site, where decreasing interatomic distance results in deeper energy levels. The valence band maxima versus the vacuum level or the IPs after atomic relaxation also show a similar trend even when other cation species and crystal structures are included in the discussion, while there is much less correlation for EAs. An overall trend indicates that lattice volume reflecting cation species is a determinant factor to the IPs of the divalent metal oxides investigated in this paper although there are surface-specific dipole contributions that cause the surface orientation dependence of the IPs.

DOI: 10.1103/PhysRevMaterials.2.124603

I. INTRODUCTION

The relative position of valence and conduction bands between semiconductors and insulators, or the band alignment, is fundamental information for surface and heterointerface design [1–5]. A comparison of the valence band maximum (VBM) and conduction band minimum (CBM) against the vacuum level or, in other words, the ionization potential (IP) and electron affinity (EA), respectively, is one approach toward determination of the band alignment between arbitrary materials. IPs and EAs are fundamentally surface dependent quantities and are affected by the surface dipole contribution [1,6,7] that depends on the atomic structure, composition, and adsorption at the surfaces. Nevertheless, IPs and EAs also provide reasonable estimates of heterojunction band alignments, especially when the constituent materials of an interface have similar crystal and electronic structures [8–10].

Systematic evaluation of IPs and EAs over a large number of systems would be useful when identifying promising surfaces and/or heterojunctions that would improve current material and/or device performance or create new functionalities. High-throughput first-principles calculations [11–21] based on density functional theory [22,23] are extremely powerful when generating a large data set of many known and hypothetical materials [17,24–26] and are widely employed to understand trends in physical and chemical properties and to explore novel materials [27–42]. Data obtained from high-throughput calculations can also be used for machine learning, which allows us to construct models for accelerated prediction of material properties [33,35,43,44].

Metal oxides play important roles in many industrial applications such as capacitors, thermistors, varistors, magnets, electronic devices, phosphors, catalysts, and photocatalysts [45–55]. Therefore, metal oxides have been targets of much experimental and theoretical investigation from viewpoints of both fundamental science and engineering technology, and experimentally known and/or theoretically favorable polymorphs are established for many oxides. For instance, the Inorganic Crystal Structure Database (ICSD) includes more than 40 000 oxides with different stoichiometries and space groups [56]. Examples of such theoretical studies include systematic first-principles investigation into binary oxide polymorphs using a variety of density functional approximations [57] as

*yoyo.hinuma@gmail.com
†oba@msl.titech.ac.jp

well as the aforementioned high-throughput computation and database construction.

In the present paper, we utilize an automated approach to systematically investigate the IPs and EAs of the nonpolar surfaces of prototypical metal oxides with divalent cations and formally closed-shell electronic structures. In addition, factors that affect the IPs and EAs are discussed. Polar surfaces are excluded because an assumption is necessary to resolve the polar instability, for example, charge accumulation, composition modulation, and/or adsorption at surfaces, which depend not only on intrinsic material characteristics but also on fabrication processes [58]. First-principles calculations are conducted using the Perdew-Burke-Ernzerhof generalized gradient approximation (GGA) functional tuned for solids (PBEsol) [59], with the Hubbard U correction [60,61] when necessary, and dielectric-dependent (dd) hybrid functionals [62–70]. It has been demonstrated that the dd hybrid functionals describe the band gaps and surface band positions well with accuracy comparable to the *GW* approximation based on many-body perturbation theory [71,72] for prototypical semiconductors and insulators but with much lower computational costs [65,66,69,73]. Systematic IP and EA evaluation at the hybrid functional level is, however, challenging as it requires a large number of surface calculations [8,74–76]. We accelerate the hybrid functional calculations using a non-self-consistent (nsc) approach, which has been shown to yield band structures similar to self-consistent solutions for a number of semiconductors and insulators [64,77,78]: for example, the difference in the band gaps of prototypical group-IV, -III–V, and -II–VI semiconductors is about 0.1 eV [73]. Moreover, the nsc approach substantially reduces the computational costs for IP and EA evaluation with reasonable accuracy preserved [73]. The advances in this paper will contribute to the acceleration of high-throughput calculations of surface properties, as well as the understanding of the factors that determine IPs and EAs.

II. METHODOLOGY

Models and procedures for first-principles calculations

Divalent metal oxides with a formally closed-shell electronic structure in nine crystal structures (prototypes) were considered. These prototypes, which also appeared in Ref. [57], are listed in Table I and visualized in Fig. 1. The considered compositions are BeO, MgO, CaO, SrO, BaO, ZnO, HgO, SnO, and PbO. CdO is excluded because the band gap for the rocksalt structure that it typically takes has a rather small band gap by PBEsol, both with and without the $+U$ corrections to the Cd $4d$ semicore states. First-principles calculations were conducted using the projector augmented-wave method [79] as implemented in the VASP code [80,81]. Among the GGAs, the PBEsol functional [59] was used because it provides reasonable energetics and crystal structures of metal oxides, for instance, compared to the standard PBE functional [82] as shown in our previous study [57]; for binary oxides, the results are comparable to the strongly constrained and appropriately normed meta-GGA that was recently proposed [83]. The nsc-dd hybrid functional calculation formalism is additionally employed to enable sufficiently accurate and computationally cost-effective IPs and EAs evaluation [73], as detailed below. The wave functions, and therefore the Hartree potential, are fixed at those obtained using PBEsol($+U$) as in the case of typical perturbative calculations such as *GW*. This nsc approach allows us to electrostatically align bulk models treated using the hybrid functional with surface models treated using PBEsol($+U$) and thereby accelerate IP and EA evaluation significantly by avoiding costly hybrid functional calculations of the surfaces.

The bulk and surface geometries were optimized using PBEsol($+U$). As an exception, the band gap of SnO is found to be sensitive to the lattice parameters, and the crystal structure relaxed using PBE was adopted to obtain a nonzero band gap for the massicot and litharge structures. The massicot structure is less stable by 57 meV/atom compared to the litharge structure. The deviations from experimental values in lattice constants a and c, respectively, are 1.5 and 3.9% with PBE and -0.1 and -2.4% with PBEsol for the litharge structure [57]. The Hubbard U correction [60,61] was additionally considered for ZnO to avoid excessive hybridization between the Zn $3d$ and O $2p$ orbitals in the valence band [19,84,85]. Dudarev's formulation [61] was used with an effective U value, U–J, of 5 eV for the Zn $3d$ orbitals. The results presented for ZnO include the Hubbard U correction unless stated otherwise as "Zn w/o $+U$." The semicore d states of Sn and Pb were considered only when calculating the Bader charges [86–89]. Bulk geometry optimization was conducted using a plane-wave basis set with an energy cutoff of 550 eV and even k-point meshes that were determined on the basis of convergence of total energies: the criterion of the total energy change was set at 0.005 meV per atom per the number of incremental k points starting from the k-point spacing smaller

TABLE I. List of prototype structures selected from the Inorganic Crystal Structure Database (ICSD) [56]. The structure type in ICSD is used as the prototype name unless indicated otherwise. Z is the number of formula units in the crystallographic conventional cell.

ICSD collection code	Space group type	Space group number	Z	ICSD structure type	Prototype
163628	$Fm\bar{3}m$	255	4	NaCl	Rocksalt
162843	$P6_3mc$	186	2	Wurtzite-ZnS (2H)	Wurtzite
29082	$F\bar{4}3m$	216	4	Sphalerite-ZnS ($cF8$)	Zincblende
18147	$P4_2/mnm$	136	4	BeO ($tP8$)	BeO
40316	$Pnma$	62	4	HgO	Montroydite
639125	$P3_121$	152	3	HgS	Cinnabar
15402	$Pbcm$	57	4	Massicot	
62842	$P4/nmm$	129	2	Litharge	
173921	$P6_3/mmc$	194	2	Nickeline-NiAs	NiAs

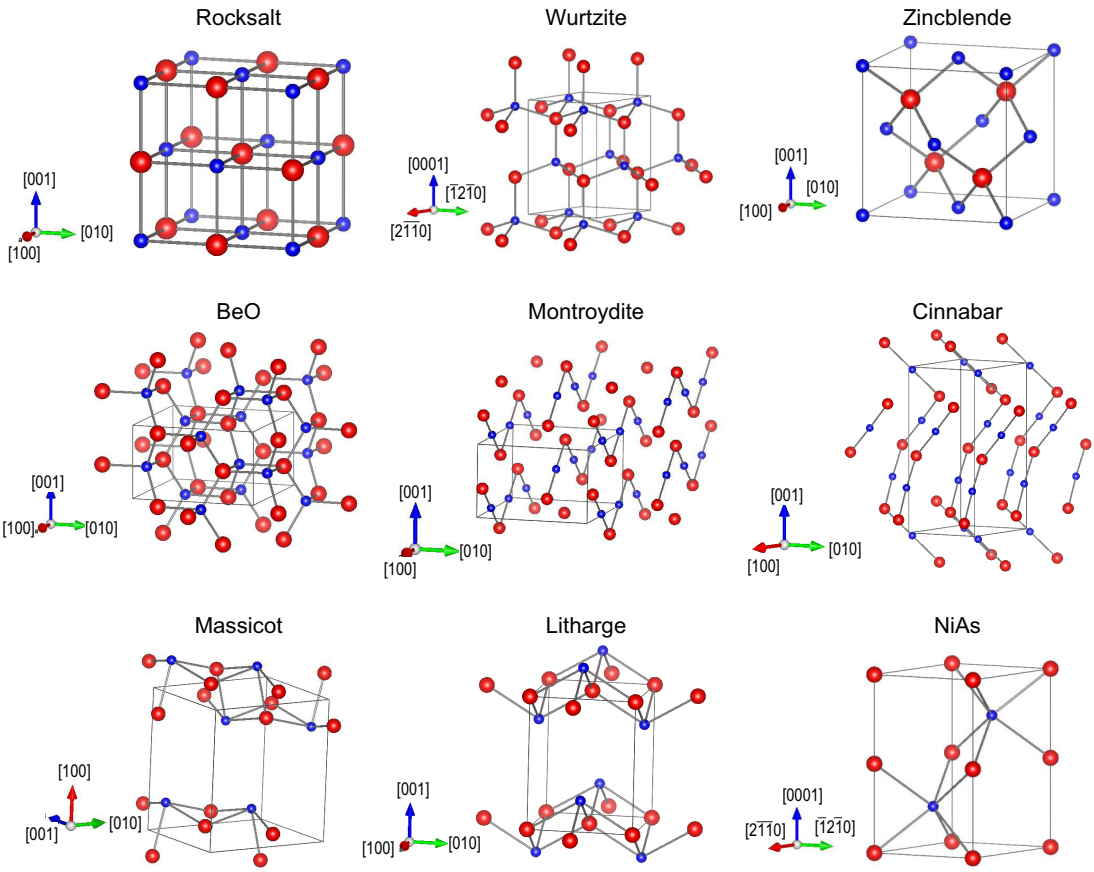

FIG. 1. Prototypes of binary oxides considered in this paper. Blue and red circles represent cations and O ions, respectively, while frames indicate unit cells.

than 0.06 Å^{-1} in the crystallographer's definition along each reciprocal basis vector.

Slab-and-vacuum models for surfaces, where slabs infinitely extending in two directions (in-plane directions) are alternated with a vacuum region in the other direction under three-dimensional periodic boundary conditions, were constructed based on the algorithm by Hinuma *et al.* [16]. Only nonpolar slabs that can be obtained by simply cleaving from bulk without substantial reconstruction were considered (nonpolar types A and B in their definition, corresponding to Tasker's types 1 and 2 [90], respectively). A set of slabs with unique termination can be automatically identified using the algorithm outlined in Appendix. All possible nonpolar and stoichiometric terminations for the same surface orientation are investigated. Surfaces with higher density of severed bonds are expected to have higher energies, hence a termination with atoms having higher coordination numbers would be favored within the same orientation. In consequence, if removing all twofold coordinated atoms near the surface results in a stoichiometric slab and threefold or higher coordination in all remaining atoms, the twofold coordinated atoms are removed to obtain a more stable surface termination within the same orientation. This process is required in some terminations such as wurtzite $(10\bar{1}0)$, $(21\bar{3}0)$, $(31\bar{4}0)$, and $(32\bar{5}0)$; BeO (100), (101), and (110); and massicot (101) and (110). Here, the coordination number is defined as the number of atoms positioned less than 1.1 times the nearest-neighbor distance. However, this atom removal process turned out to always result in another termination that was already found, thus additional consideration of this reconstruction was not necessary for the surfaces dealt with in the present paper.

IPs and EAs were calculated based on the bulk-based definition [91] that excludes the explicit effects of in-gap surface states as in typical IP and EA evaluation [19]. In this approach, the IP (I) and EA (A) are obtained by combining surface and bulk calculations as [19,91]

$$I = \varepsilon_{\text{vac}}^{\text{surface}} - \varepsilon_{\text{ref}}^{\text{surface,far}} - \left(\varepsilon_{\text{VBM}}^{\text{bulk}} - \varepsilon_{\text{ref}}^{\text{bulk}}\right), \tag{1}$$

$$A = \varepsilon_{\text{vac}}^{\text{surface}} - \varepsilon_{\text{ref}}^{\text{surface,far}} - \left(\varepsilon_{\text{CBM}}^{\text{bulk}} - \varepsilon_{\text{ref}}^{\text{bulk}}\right). \tag{2}$$

A surface calculation using a slab model (supercell) is used to obtain $\varepsilon_{\text{vac}}^{\text{surface}}$ and $\varepsilon_{\text{ref}}^{\text{surface,far}}$, which are the vacuum level and the reference level in the bulklike region far from the surface, respectively. The bulklike region is defined as the middle one-third of the slab. On the other hand, a bulk calculation is used to determine $\varepsilon_{\text{VBM}}^{\text{bulk}}$, $\varepsilon_{\text{CBM}}^{\text{bulk}}$, and $\varepsilon_{\text{ref}}^{\text{bulk}}$, which are the VBM, CBM, and the reference level, respectively.

The IPs and EAs, as well as the band gaps, were corrected from PBEsol($+U$) values using the nsc-dd hybrid functional calculations for the bulk models [73]. The average local potential at the atomic sites was used as the reference level. The reciprocal of the electronic contribution to the static

dielectric constant was used as the amount of the nonlocal Fock-exchange mixing in the full-range dd-hybrid functional, which is identical to the PBE0 hybrid functional except for the nonlocal exchange mixing value [63,66,73]. PBEsol(+U) and the random-phase approximation (RPA) were used to evaluate the electronic static dielectric constants based on the density functional perturbation theory (DFPT) [92,93], which has been shown to yield values close to experimental electronic static dielectric constants [19,73]. The number of k points sampled in the DFPT calculations was increased by 2.5 times in all the directions from the k mesh used in the bulk geometry optimization stage. The convergence of IPs and EAs was checked by building slabs of the same termination with various thicknesses and incrementally increasing the thickness by the minimum possible amount until the changes in the IP and EA are less than 0.1 eV per inclement. The resultant slab thickness is larger than 15 Å and three repeat units, and the minimum vacuum thickness is 12 Å.

III. RESULTS AND DISCUSSION

A. Bulk electronic structure and properties

Table II shows the minimum and direct band gaps of binary divalent metal oxide polymorphs obtained using PBEsol(+U). Values are not shown for crystals with significant lattice or internal coordinate (IC) relaxation (lattice deformation index $LR_2 > 0.2$ and/or IC relaxation index $CR > 0.25$ Å; the definitions of LR_2 and CR are found in Ref. [57]) or those that are metastable by 0.05 eV/atom or more compared to the lowest-energy polymorph (hereafter denoted as "highly metastable" while polymorphs metastable by 0.05 eV/atom or less are defined as "slightly metastable"); the relative formation energies of polymorphs have been reported in Ref. [57]. Exceptions are made for some rocksalt, wurtzite, and zincblende structure systems that are highly metastable and considered to investigate the crystal structure dependence of IPs and EAs.

The electronic static dielectric constants obtained using PBEsol(+U) and the RPA are listed in Table III and compared with available experimental values [94,95]. The theoretical values are reasonably close to the corresponding experimental values, as is also found in other semiconductors and insulators treated using PBE(+U) and the RPA in Refs. [19,73]. The overestimating tendency is partly attributed to the underestimation of the band gaps by PBEsol(+U). A wider gap material tends to yield a smaller dielectric constant, resulting in a larger contribution of the nonlocal Fock exchange in the dd-hybrid functional. Here, a dielectric constant of 4 corresponds to 25% nonlocal exchange mixing that is adopted in HSE06 [96–98] and PBE0 [99–101].

Table IV shows the minimum and direct band gaps obtained using nsc-dd hybrid functional calculations. The effect of including spin-orbit coupling (SOC) on the band gap was investigated for oxides containing heavy cations, namely, litharge and massicot PbO as well as cinnabar and montroydite HgO. The band-gap reduction by including SOC is less than 0.1 eV for both PbO and HgO, and therefore this effect is not considered in this paper. Table V compares the theoretical band gaps of selected systems with experimental values. It is found that the nsc-dd hybrid functional results show a significant improvement over those of PBEsol(+U) for closed-shell binary metal oxides considered in this paper, as is the case for group-IV, -III–V, and -II–VI semiconductors [73].

Figures 2 and 3 show the electronic density of states (DOS) and band structure of selected systems obtained using nsc-dd hybrid functional calculations, respectively. The results for three types of crystal structures are shown for MgO and ZnO to discuss the structure dependence. The electronic structures of rocksalt MgO, CaO, SrO, and BaO near the band gaps are relatively simple; the electronic states near the VBM are

TABLE II. Minimum and direct band gaps of divalent metal oxides from PBEsol(+U) calculations (in eV). Values in italics are for highly metastable polymorphs. A system has a direct-type band structure when its direct gap is the same as the minimum gap; otherwise, the band structure is of indirect type and the direct band gap is shown in parentheses.

	BeO	MgO	CaO	SrO	BaO	ZnO w/o +U	ZnO	HgO	SnO	PbO
Rocksalt	*8.25* (*8.54*)	4.66	3.55 (3.91)	3.16 (3.25)	1.86	*0.81* (*2.21*)	*1.86* (*2.88*)			
Wurtzite	7.47	*3.38*				0.68	1.46			
Zincblende	6.68 (7.43)	*3.50*	*3.26* (*3.92*)	*2.44* (*3.34*)	*2.22* (*3.44*)	0.57	1.35			
BeO	7.08 (7.10)					0.68	1.47			
Montroydite								1.11 (1.50)		
Cinnabar								1.19 (1.31)		
Massicot										1.98 (2.22)
Litharge									0.37 (1.86)	1.18 (2.21)
NiAs					2.30 (2.36)					

TABLE III. Electronic contribution to the spherically averaged dielectric constants of divalent metal oxides obtained using PBEsol(+U) and the RPA. Values in italics are for highly metastable polymorphs. Experimental values from Refs. [94,95] are shown in parentheses.

	BeO	MgO	CaO	SrO	BaO	ZnO w/o +U	ZnO	HgO	SnO	PbO
Rocksalt	*3.51*	2.99 (2.9,[a] 3.1[b])	3.65 (3.3[b])	3.67 (3.3[b])	4.13 (3.6[b])	*5.23*	*4.58*			
Wurtzite	2.96	*2.83*				5.17 (3.7[a])	4.12 (3.7[a])			
Zincblende	2.97	*2.88*	*3.14*	*3.22*	*3.67*	5.58	4.22			
BeO	2.89					4.84	3.96			
Montroydite								6.05		
Cinnabar								6.11		
Massicot										6.69
Litharge									6.71	6.12
NiAs					4.44					

[a]Reference [94].
[b]Reference [95].

mainly composed of the O 2p states. The valence band width decreases in the order of MgO, CaO, SrO, and BaO, which can be partly attributed to the O-O distance that increases in this order. The primary contributors around the CBM are cation s states for MgO and ZnO, whereas the d-state contributions are prominent in CaO, SrO, and BaO. The semicore cation p band moves upward as the cation becomes heavier from CaO (~ -20 eV) to BaO (~ -11 eV). Hybridization between these cation p states and the O 2s states is especially noticeable in CaO and SrO. ZnO is more complicated as the semicore Zn 3d states are energetically close to the O 2p states and they hybridize largely with each other. Both cation s and p states hybridize significantly with the O 2p states near the VBM in SnO, PbO, and HgO; the contribution of the Hg 5d states is also recognized in the valence band of HgO.

Turning to the crystal structure dependence in MgO and ZnO, the overall chemical features in the band structures are common to the polymorphs for each compound, although differences in the relative band position and band width are recognized. In addition, the band structure is of indirect type for rocksalt ZnO whereas all the other polymorphs of MgO and ZnO are of direct type. Here, note that the primitive cell of the wurtzite structure contains four atoms compared to two in the rocksalt and zincblende, thus the band diagram of wurtzite contains double the number of bands of rocksalt and zincblende.

B. Surface electronic structure and energetics

As an example of the results on the surface band alignment, Fig. 4 shows the VBM and CBM with respect to the vacuum

TABLE IV. Minimum and direct band gaps of divalent metal oxides from nsc-dd hybrid functional calculations (in eV). Values in italics are for highly metastable polymorphs. A system has a direct-type band structure when its direct gap is the same as the minimum gap; otherwise, the band structure is of indirect type and the direct band gap is shown in parentheses.

	BeO	MgO	CaO	SrO	BaO	ZnO w/o +U	ZnO	HgO	SnO	PbO
Rocksalt	*11.40* (*11.72*)	8.02	6.48 (6.89)	5.85 (5.94)	4.06	*2.72* (*3.89*)	*3.48* (*4.92*)			
Wurtzite	11.10	*6.72*				2.61	3.28			
Zincblende	10.23 (11.06)	*6.81*	*6.20* (*6.84*)	*5.22* (*6.15*)	*4.58* (*5.89*)	2.36	3.10			
BeO	10.75 (10.77)					2.75	3.36			
Montroydite								2.30 (2.79)		
Cinnabar								2.33 (2.47)		
Massicot										3.00 (3.19)
Litharge									1.07 (2.67)	2.15 (3.29)
NiAs					4.39 (4.44)					

TABLE V. Comparison of calculated and experimental band gaps (in eV). No direct band-gap value is given if it is the same as the minimum gap. Experimental values are taken from Refs. [102–111].

		Minimum band gap		Direct band gap		
System	Prototype	PBEsol ($+U$)	nsc-dd hybrid	PBEsol ($+U$)	nsc-dd hybrid	Experiment
BeO	Wurtzite	7.47	11.10			9.9,[a] 10.6[b]
MgO	Rocksalt	4.66	8.02			7.833 ± 0.020[c]
CaO	Rocksalt	3.55	6.48	3.91	6.89	5.7,[a] 7.085 ± 0.020,[c] 7.085 (Γ),[d] 7.47 (X),[d] 7.16 (L)[d]
SrO	Rocksalt	3.16	5.85	3.25	5.94	6.1,[a] 5.896 (Γ),[d] 6.28 (X),[d], 5.97 (L)[d]
BaO	Rocksalt	1.86	4.06			4.8,[a] 4.286 (Γ),[d] 4.182 (X),[d], 3.89 (L),[d] 4.2 ± 0.1[e]
ZnO	Wurtzite	1.46	3.28			3.4,[a] 3.44[f]
HgO	Montroydite	1.11	2.30	1.50	2.79	2.19, 2.80[g]
SnO	Litharge	0.37	1.07	1.86	2.67	0.7 (indirect), 2.7 (direct)[h]
PbO	Litharge	1.18	2.15	2.21	3.29	1.9 ± 0.2[i]
PbO	Massicot	1.98	3.00	2.22	3.19	2.5[j]

[a]Reference [102]; [b]Ref. [103]; [c]Ref. [104]; [d]Ref. [105]; [e]Ref. [106]; [f]Ref. [107]; [g]Ref. [108]; [h]Ref. [109]; [i]Ref. [110]; [j]Ref. [111].

level (the negatives of the IP and EA, respectively) for selected nonpolar surfaces of stable and slightly metastable structures after IC relaxation, obtained using nsc-dd hybrid functional calculations. Both $(10\bar{1}0)$ and $(2\bar{1}\bar{1}0)$ surfaces are considered for the wurtzite structure. The results are compared with available experimental values for the same surface orientations [109,112–114]. The band positions of rocksalt MgO and wurtzite ZnO are relatively well reproduced, whereas those of litharge SnO are predicted to be ~ 1 eV higher. The discrepancy from the experimental value would partly result from the difference in the detail of the local chemical composition and structural reconstruction at the surface. The theoretical IP of the ZnO wurtzite $(10\bar{1}0)$ surface with IC relaxation is 7.61 eV, which is slightly smaller than the experimental value of 8.0 eV [114]. The $(2\bar{1}\bar{1}0)$ surface shows a similar theoretical IP of 7.64 eV, while a reported experimental value is 7.82 eV [113].The surface orientation dependence is not significant for these nonpolar surfaces of ZnO in both theory and experiment. It is noted that the slight errors in theoretical lattice constants, -2.3 and -1.8% for a and c, respectively, affect the IP; for instance, fixing the lattice parameters to experimental values and then relaxing ICs increases the IP by about 0.2 to 7.85 eV for the $(10\bar{1}0)$ surface.

A chemical tendency is recognized in the band positions within the same crystal structures, namely, between MgO, CaO, SrO, and BaO in the rocksalt structure and BeO versus ZnO in three kinds of structures. In particular, the tendency in the VBM or IP of the rocksalt crystals is consistent with a previous theoretical study by Logsdail *et al.*, where surface polarization effects are considered in the evaluation of the band positions [115]. For further discussion, the effect of each factor, such as the crystal structure and chemical composition, needs to be differentiated. Therefore, in the following section we focus mainly on three crystal structures, which are rocksalt, zincblende, and wurtzite, and six compositions, namely, BeO, MgO, CaO, SrO, BaO, and ZnO. Many of the combinations of these crystal structures and compositions are experimentally found and/or theoretically predicted to have relatively low energies [57].

1. Prototypical rocksalt, zincblende, and wurtzite surfaces

The rocksalt (100), zincblende (110), and wurtzite $(10\bar{1}0)$ surfaces are selected as prototypical surfaces and their properties are investigated for BeO, MgO, CaO, SrO, BaO, and ZnO. Of these, wurtzite CaO, SrO, and BaO are not discussed here because these bulk crystals relax considerably toward hexagonal BN-like layered structures from the original wurtzite structures.

Figure 5 shows the band positions of these prototypical surfaces alongside their band gaps. The VBM and CBM with respect to the vacuum level are plotted in the vertical axis of the middle and upper panels, which are the negatives of IPs and EAs, respectively. Calculations were conducted with and without relaxation of ICs in slab calculations ("IC relaxed" and "IC fixed," respectively) to investigate the relaxation effects. The band gap decreases as the cation goes down the periodic table within the same group and crystal structure, which is a well-known chemical trend. The VBM shifts upward toward the vacuum level (the IP decreases) as well, and a possible cause of this observation is discussed later. Similarly, the CBM shifts downwards (the EA increases) for the rocksalts and wurtzites, but the change is not as smooth as that of the VBM. The zincblendes show somewhat different behaviors. These results can be understood from the fact that the VBM is composed primarily of the O $2p$ states in all systems, together with some minor contribution from cationic semicore states, whereas the main contributors to the CBM are cationic states showing various low-lying orbital symmetry and spatial distribution.

Relaxation of ICs in slab calculations tends to shift the VBM downward from the vacuum level (increase the IP) when the constituent cation is lighter and/or smaller in ionic size, which is evident in Fig. 6 where results for the rocksalt (100) surfaces and the zincblende (110) surfaces are plotted; the results for the wurtzite $(10\bar{1}0)$ surfaces are almost the same as those for the zincblende (110) surfaces and are therefore omitted from Fig. 6. All prototypical surfaces are of type A by Hinuma *et al.*'s definition [16], or type 1 by Tasker's definition [90], which means that all layers are stoichiometric and thus have zero net charge in the point charge picture

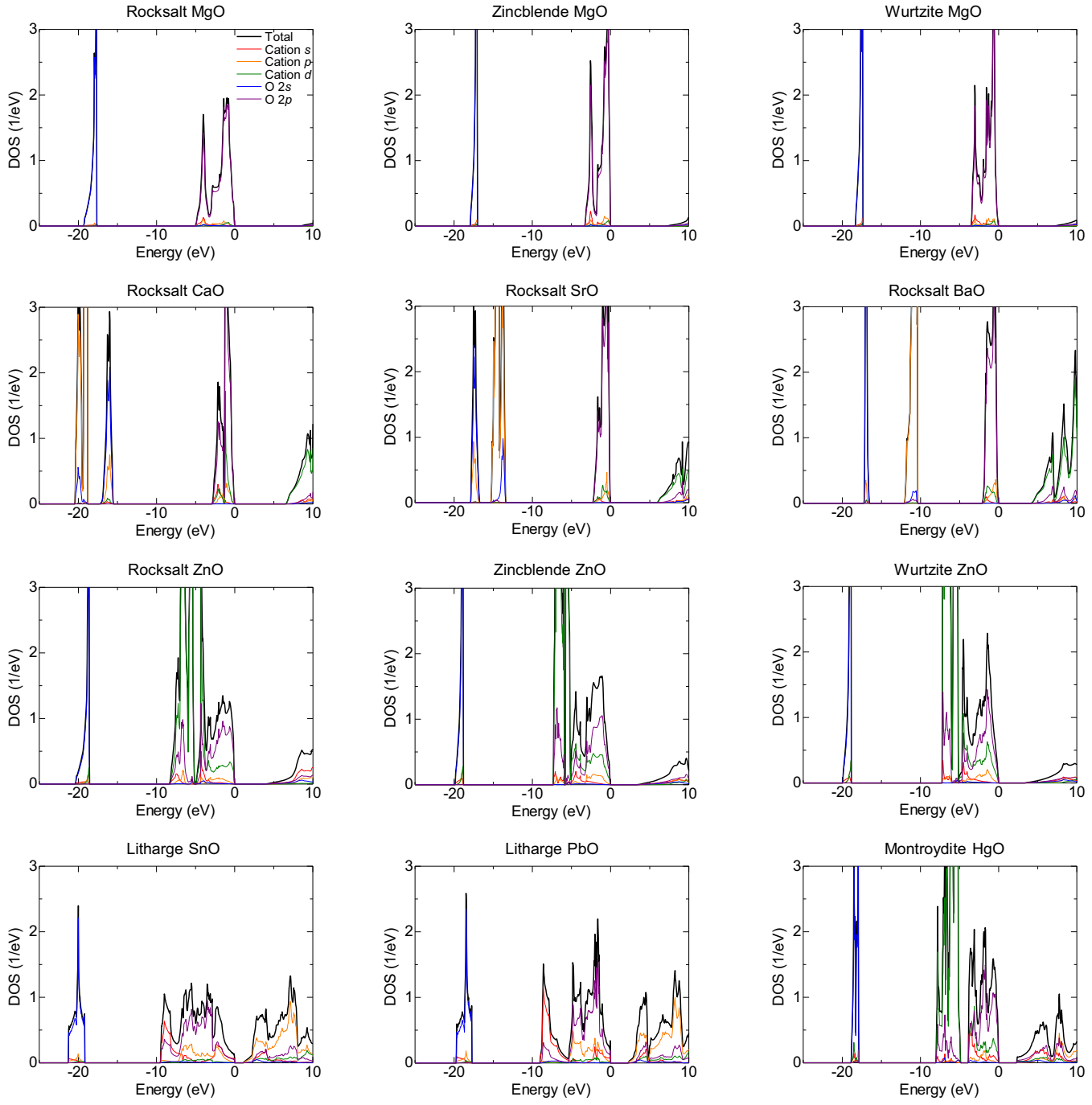

FIG. 2. Electronic density of states (DOS) of selected systems from nsc-dd hybrid functional calculations. The total and orbital projected DOS are shown in eV^{-1}/f.u. and eV^{-1}/atom, respectively. Energies are taken with respect to the VBM.

prior to relaxation, aside from a slight charge transfer from the surface layer to the inner layers. However, cations and anions relax differently along the direction perpendicular to the surface, and the topmost layer, together with other layers, separates into two charged layers. The relaxation changes the VBM position (the IP) by up to ∼1 eV in BeO. Figure 7 plots the relative displacement in the direction perpendicular to the surface between cation and anion layers that are closest to the surface against the difference in the VBM (and also the CBM) when ICs are fixed and relaxed in the slab calculations. A positive value of the relative displacement means that the cation layer is closer to vacuum than the O ion layer. There is a strong correlation between this relative displacement and the change in the VBM (the negative of the IP) with relaxation, which can be qualitatively explained by simple electrostatics. The cation and anion layers closest to the surface may be modeled as uniformly charged planes that act as two plates of a parallel plate capacitor, where the charge density on each plane is estimated using the formal ionic charges of ±2 (see Fig. 8). Looking from the vacuum side, the potential of the slab side becomes lower when the anion layer is closer to vacuum. This translates to a downward shift of the VBM

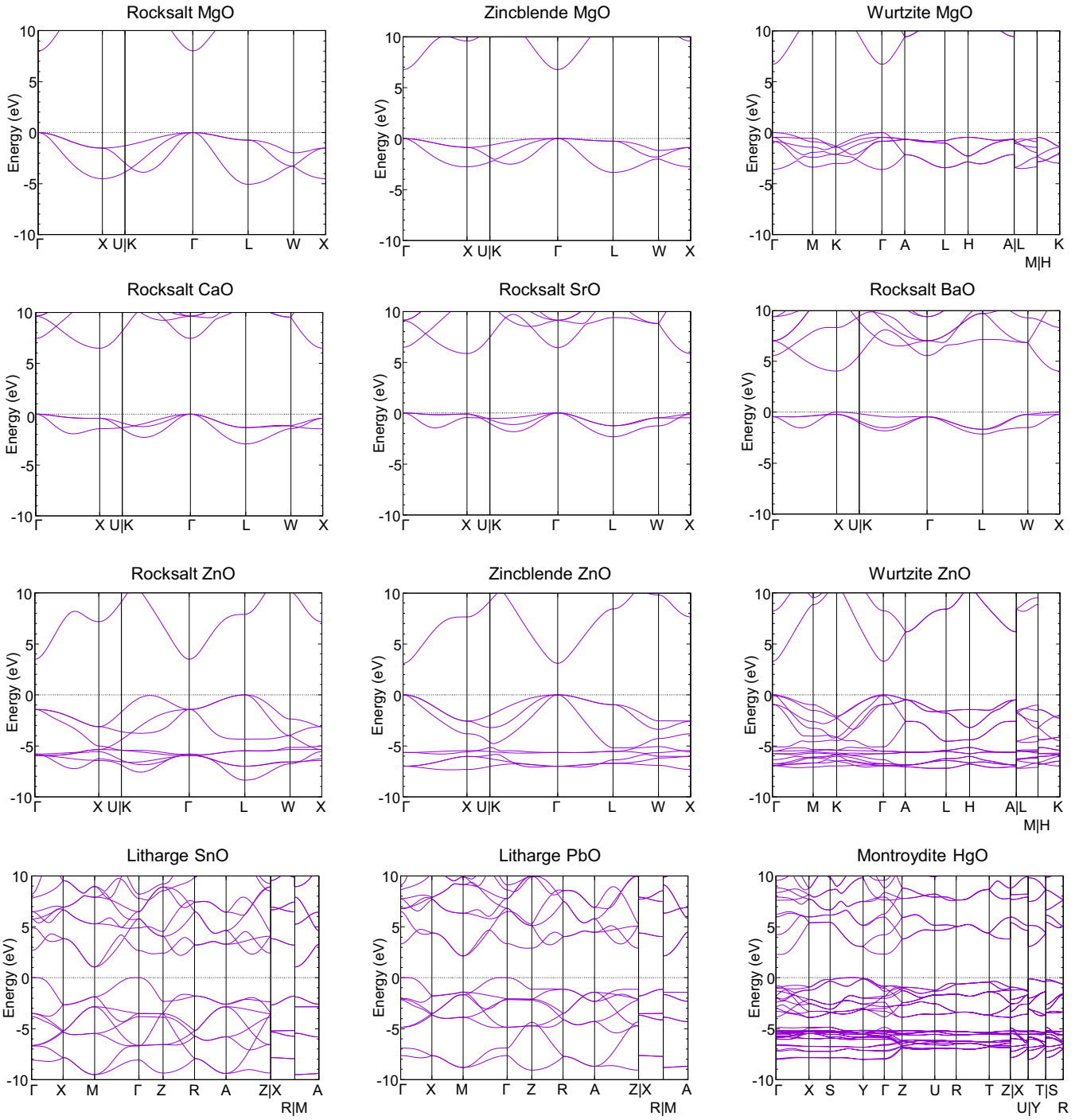

FIG. 3. Electronic band-structure diagrams of selected systems from nsc-dd hybrid functional calculations. Band paths are based on those reported in Ref. [15]. Energies are taken with respect to the VBM.

with relaxation [116]. The second set of layers relaxes in the direction opposite from the first (outermost) set of layers, thereby canceling out some of the VBM shift. There should be contributions from layers farther away from the surface but the contributions are expected to become smaller as the distance from the surface increases. The results shown in Fig. 7 indicate that the VBM position (the negative of the IP) is relatively insensitive to the atomic relaxation for zincblende ZnO with respect to MgO having a similar lattice constant (and the wurtzite as well, for which the results are not shown in Fig. 7). This behavior may be partly attributed to the relatively small net charges of the constituent Zn and O ions; the calculated Bader charges in the rocksalt structure are ± 1.77, ± 1.72, ± 1.54, ± 1.47, ± 1.44, and ± 1.32 times the elementary charge for BeO, MgO, CaO, SrO, BaO, and ZnO, respectively. The absolute values for the zincblende structure are smaller only by 0.01 to 0.04 times the elementary charge.

Figure 9 plots the VBM (negative of the IP), O 2*s* band center versus the vacuum level, average local potential energy for an electron at the O site with respect to that for an isolated

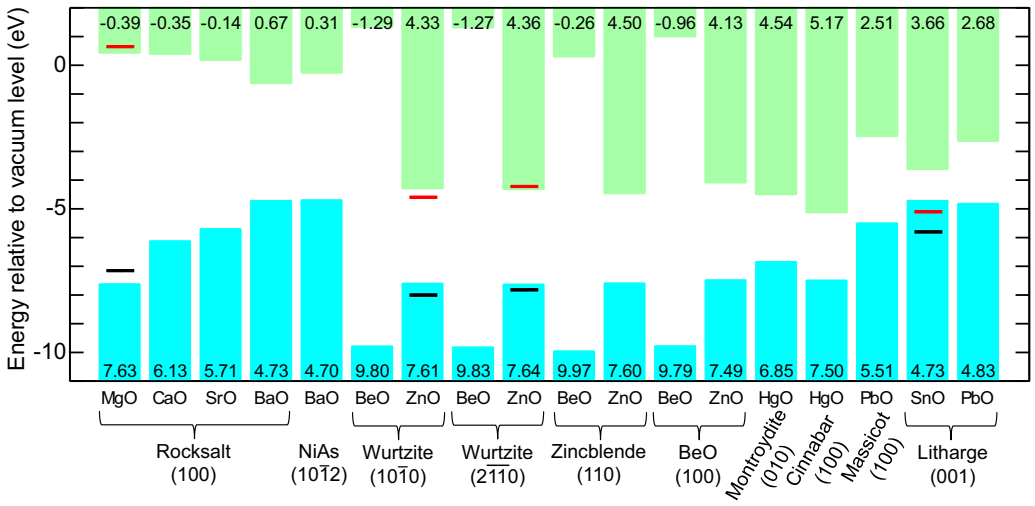

FIG. 4. VBM and CBM with respect to the vacuum level (the negatives of the IP and EA, respectively) for selected nonpolar surfaces of stable and slightly metastable systems from nsc-dd hybrid functional calculations; the IP and EA values are indicated at the bottom and top of the figure, respectively. Relaxation of atomic positions, i.e., internal coordinates, is taken into account in surface calculations. The horizontal black and red bars represent experimental IP and EA values taken from Refs. [109,112–114], respectively.

O atom in vacuum, and Madelung potential energy for an electron at the O site against the reciprocal of the cube root of volume per atom; the volume per atom is obtained by dividing the primitive cell volume by the number of atoms in the cell and its cube root is exactly (nearly) proportional to the interatomic distance for the rocksalt and zincblende (wurtzite) structures. Highly metastable structures are included to contain as many samples as possible. Relaxation of ICs is not performed because highly metastable structures tend to relax excessively and this behavior adds another degree of complexity when looking for trends. The O $2s$ band center was obtained by calculating the atom-projected DOS of O and then taking a weighted average from -22 to -9 eV below the VBM. Choosing this range allows averaging over the entire O $2s$ band in all the considered systems for both PBEsol($+U$) and nsc-dd hybrid functional results.

All of the parameters considered in Figs. 9(a)–9(c) gradually decrease with the decrease in volume from BaO to BeO, which is especially visible when viewed within the same crystal structure. This implies the presence of an electrostatic origin behind the observed tendency. We therefore consider the Madelung potential energy for an electron at the O site $E_{\mathrm{M}}^{\mathrm{ele}}$, which is given for the rocksalt and zincblende structures (and also the idealized wurtzite structure) as

$$E_{\mathrm{M}}^{\mathrm{ele}} = -\frac{\alpha q e^2}{4\pi\varepsilon_0 r_0} \tag{3}$$

where α is the Madelung constant that depends on the crystal structure, q (>0) is the dimensionless ionic charge, e is the elementary charge, ε_0 is the vacuum permittivity, and r_0 is the nearest-neighbor distance. For the nonpolar type-A, or Tasker's type-1, surfaces, the Madelung potential for the three-dimensional systems would provide a reasonable estimate of electrostatic potential effects since the direct summation of point charges in real space converges well when the summation is terminated by such surfaces [117]. Note that the vacuum potential is then exactly zero.

Assuming constant ionic charges over different cations, $E_{\mathrm{M}}^{\mathrm{ele}}$ will appear as a (nearly) straight line against the reciprocal of r_0 for the rocksalt and zincblende (wurtzite) structures. This is illustrated in Fig. 9(d). The Madelung potential energies for the wurtzite structures are numerically calculated for the actual crystal structures using the Ewald method as implemented in the PYMATGEN code [11], but these values are found to be different by only less than 0.1 eV from the idealized crystal structure values. Defining the volume per atom as v, its cube root $v^{1/3}$ is (nearly) proportional to r_0 in each structure considered here, and therefore substituting $v^{1/3}$ for r_0 simply results in a different proportionality coefficient. The former ($v^{1/3}$) is chosen because the latter (r_0) is not a ubiquitously applicable description of the geometry of a crystal and, even worse, hinders direct comparison between crystals with different coordination environments. As discussed later, Madelung potential energies explicitly calculated using actual crystal structures also well correlate with $v^{1/3}$ for various crystal structures including those other than the rocksalt, zincblende, and wurtzite.

The VBM, O $2s$ band center, and O-site local potential energy all qualitatively follow the tendency in the Madelung potential energy where decreasing interatomic distance results in deeper positions. Among them, the VBM would be affected by factors other than electrostatics more than the O $2s$ band center and local potential energy. For instance, the valence band width changes with the cation species, as well as the crystal structure, as discussed above. This effect is expected to reduce the tendency of the VBM to go down from BaO to BeO as the band width increases in this order. In addition, hybridization of the Zn $3d$ states into the O $2p$-based valence band of ZnO, as well as its relatively small net charges and therefore weaker Madelung potential, could explain the higher VBM than that expected from the trend in Fig. 9(a); the lattice volume of ZnO is close to that of MgO in each crystal structure, but the VBM of ZnO is clearly higher. To differentiate the effects of the Zn $3d$ position and the lattice parameters in

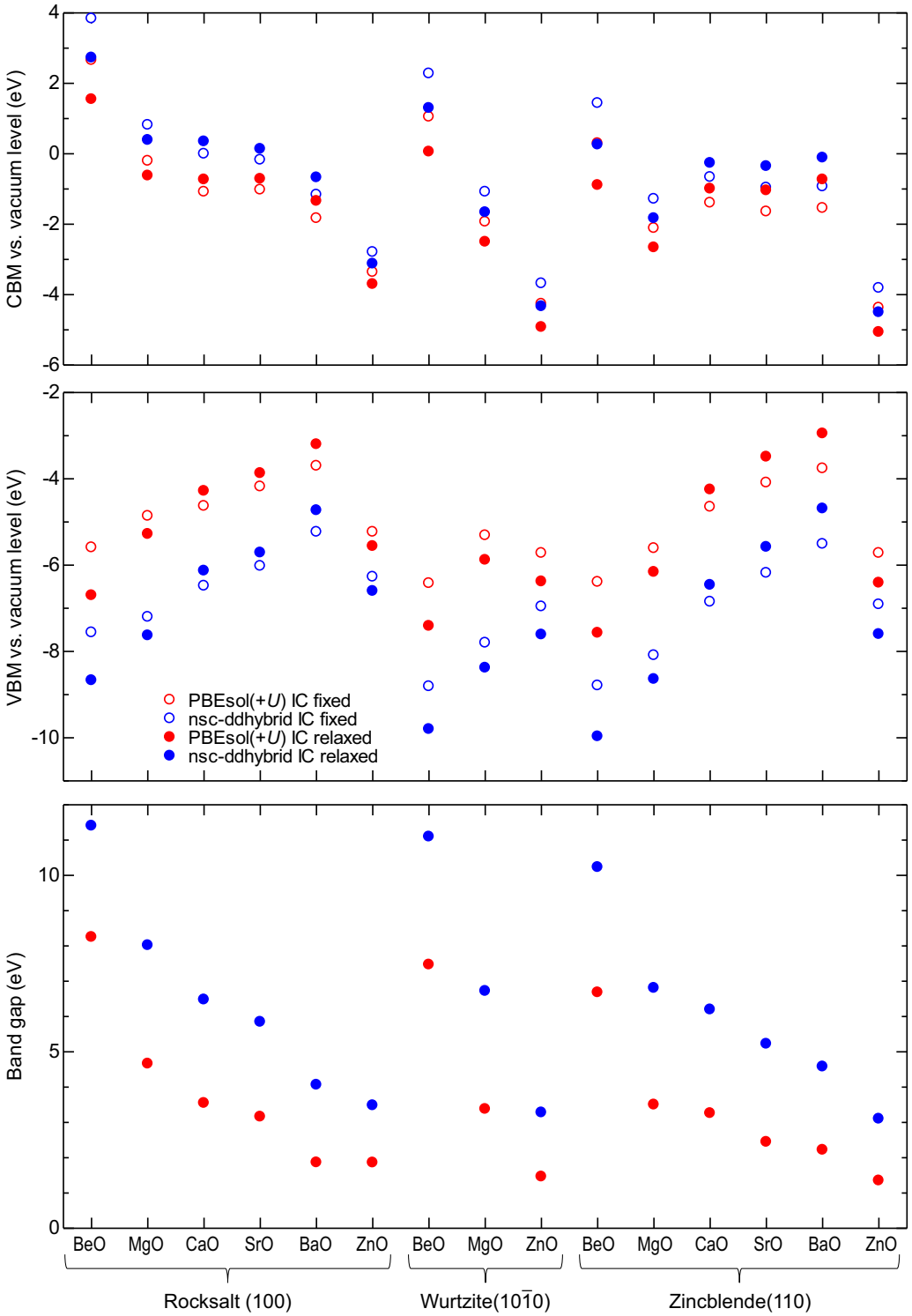

FIG. 5. CBM and VBM with respect to the vacuum level (the negatives of the EA and IP, respectively) and band gaps of prototypical surfaces for three types of crystal structures. Atomic positions, i.e., internal coordinates (ICs), are fixed and relaxed during the surface calculations in IC fixed and IC relaxed, respectively.

ZnO, both of which change by the $+U$ correction to the Zn $3d$ states, PBEsol$+U$ calculations are also performed using PBEsol lattice parameters. As a result, the $+U$ correction is found to lower the VBM by 0.2–0.4 eV for the three crystal structures under the common PBEsol lattice parameters, while the changes in the O 2s band center are less than 0.1 eV. Therefore, the relatively high VBM of ZnO is partly attributed to the Zn $3d$-O $2p$ hybridization.

The O $2s$ band center shows an almost linear trend in all the crystals [Fig. 9(b)]. However, the value for ZnO, which is the only system with valence d states, is about 2 eV lower than the trend formed by other crystals with PBEsol($+U$). Such a

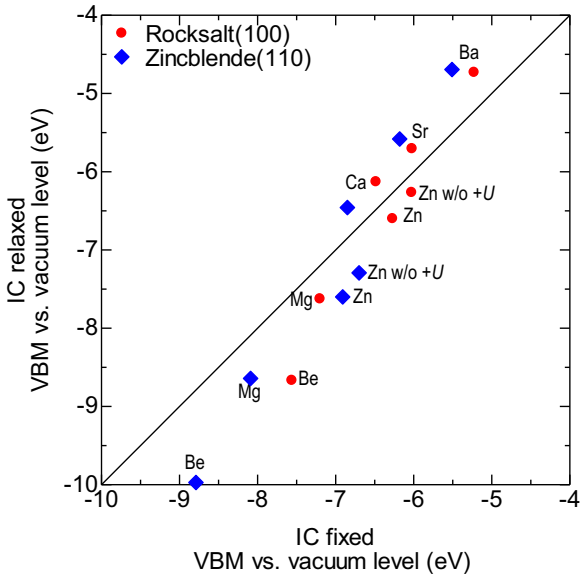

FIG. 6. Relation of the VBM with respect to the vacuum level (the negative of the IP) between when internal coordinates (ICs) are fixed and relaxed during surface calculations. The values are from nsc-dd hybrid functional calculations but the changes in the VBM by IC relaxation are the same for PBEsol(+U) as the surfaces are treated using PBEsol(+U) in both cases.

significant deviation is not noticeable with the nsc-dd hybrid functional results. Similarly, ZnO also shows a deviation from the trend in the O-site local potential energy, which is treated using PBEsol(+U) [Fig. 9(c)]. Possible causes for these deviations are the Zn-3d hybridization and/or smaller net charges than the other oxides. Both O 2s band center and O-site local potential energies do not show significant crystal

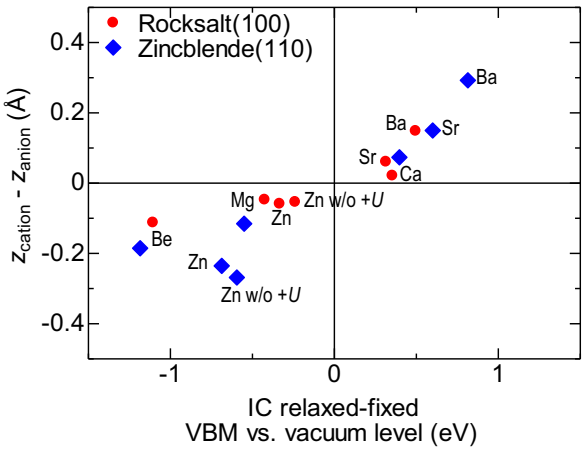

FIG. 7. Relative displacement between topmost cation and anion layers in the direction perpendicular to the metal oxide surface (positions denoted as z_{cation} and z_{anion}, respectively) vs the difference in the VBM with respect to the vacuum level (the negative of the IP) when internal coordinates (ICs) are fixed and relaxed during surface calculations. A positive value along the vertical axis indicates that the cation layer is closer to vacuum, while a positive value along the horizontal axis means that the VBM goes up toward the vacuum level when ICs are relaxed.

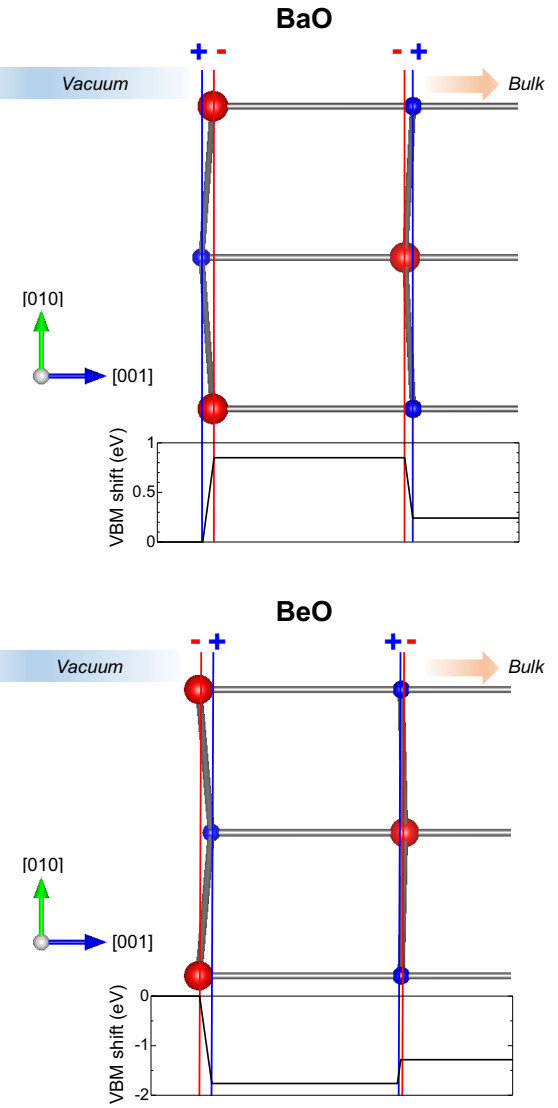

FIG. 8. Relaxation of atoms at the (100) surfaces in rocksalt BaO and BeO along with the VBM shift based on the uniform sheet charge and parallel plate capacitor model. Blue and red circles represent cations and O ions, respectively. The direction perpendicular to the surface is taken to be [001] and the surface plane is (001) in the figure.

structure dependences, despite the crystal volume and coordination number differences between rocksalt and the others. The maximum difference between polymorphs is 0.6 eV in ZnO without +U followed by 0.5 eV in CaO in both O 2s band center (PBEsol) and relative O site local potential energy. From another viewpoint, rocksalt results tend to yield higher O 2s band centers than those expected from the volume dependence. Smaller volume per atom for rocksalts than wurtzites and zincblendes would increase the repulsive interaction between neighboring O 2s states. A similar effect, as well as the band width and hybridization effects discussed above, may contribute to the determination of the O 2p-derived VBM shown in Fig. 9(a). The trend where the VBM, O 2s band center, and O-site local potential energy decrease with increasing $v^{-1/3}$ [Figs. 9(a)–9(c), respectively] is consistent

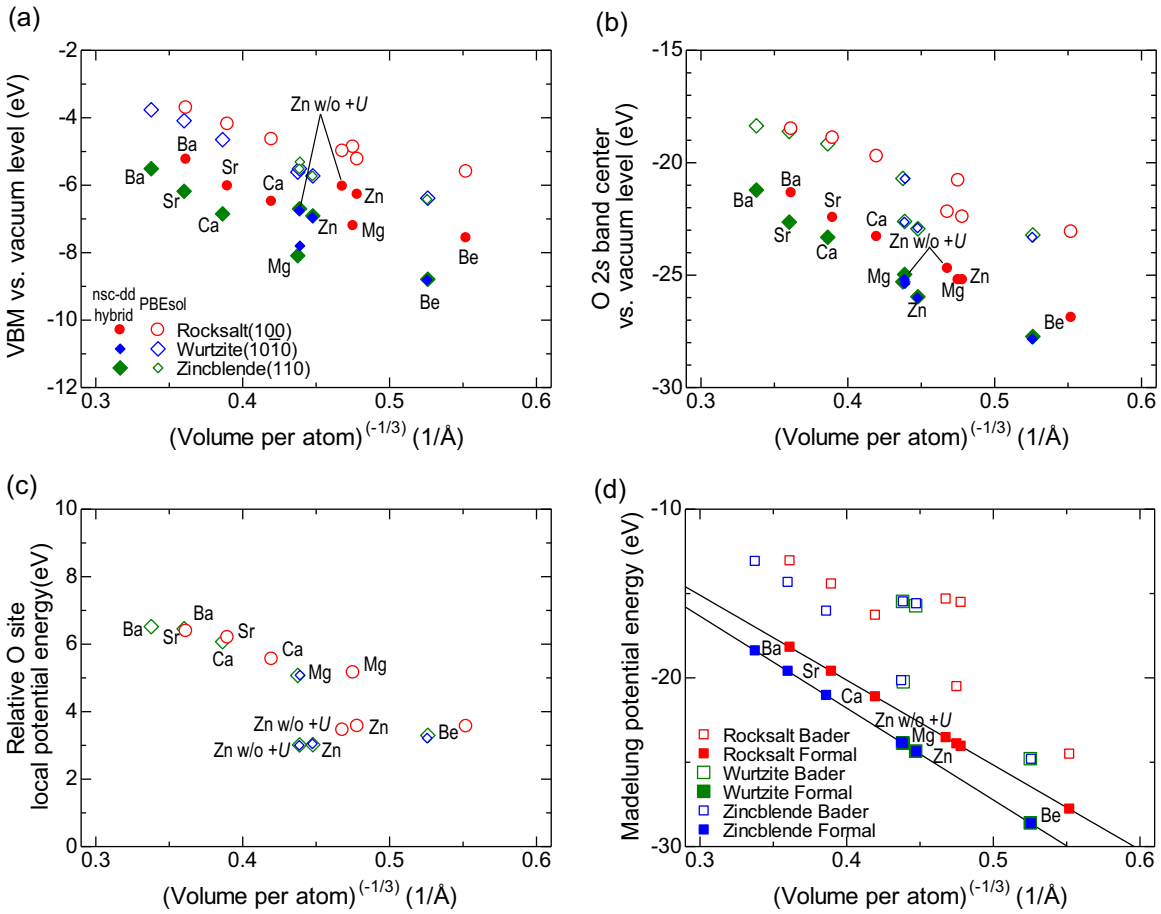

FIG. 9. (a) VBM with respect to the vacuum level (the negative of the IP), (b) O 2*s* band center vs the vacuum level, and (c) average local potential energy for an electron at the O site in the bulklike region of the slab model with respect to an isolated O atom in vacuum. The values are shown for the rocksalt, zincblende, and wurtzite structures. The O 2*s* band center corresponding to that in the bulklike region of the slab model is estimated using the combination of bulk and surface results as in the case of the VBM (IP) evaluation. (d) Madelung potential energy for an electron at the O site, based on Bader or formal charges. Note that the formal charge points lie exactly (nearly) on the line for the rocksalts and zincblendes (wurtzites), and that the wurtzite values are almost identical to the zincblende values. In (a)–(d), the values are plotted against the reciprocal of the cube root of volume per atom, which is (nearly) proportional to the reciprocal interatomic distance for the rocksalt and zincblende (wurtzite) structures. Internal coordinates are fixed in surface calculations.

with the Madelung potential energy [Fig. 9(d)] although the slope cannot be quantitatively reproduced with either formal or Bader charges. The discrepancies are attributed to the fact that the O 2*s* states show a finite spatial distribution and the O-site local potential energies are evaluated within a finite-sized sphere in contrast to the point charges in the formula of the Madelung potential energy. In addition, the O 2*s* band center and O-site local potential energy involve contributions other than such a simple electrostatics; in particular, the former is affected by the energy contributions associated with all the terms in the one-electron Hamiltonian.

2. *Surfaces of stable and slightly metastable polymorphs of binary divalent metal oxides*

Our discussion is now extended to the trend of all the stable and slightly metastable oxide polymorphs shown in Fig. 4; additional nonpolar surfaces selected based on the rule given in the Methodology section are also considered here. Figure 10 shows the VBM with respect to the vacuum level

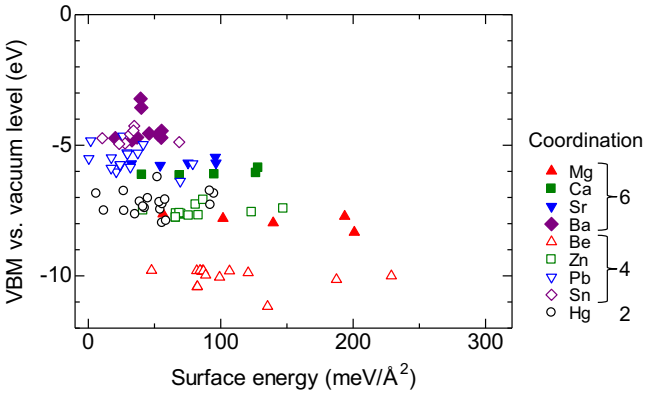

FIG. 10. VBM with respect to the vacuum level (the negative of the IP) vs surface energy for stable and slightly metastable divalent metal oxide polymorphs. The VBM refers to the values from nsc-dd hybrid functional calculations while the surface energy is obtained using PBEsol(+*U*). Internal coordinates are relaxed in surface calculations.

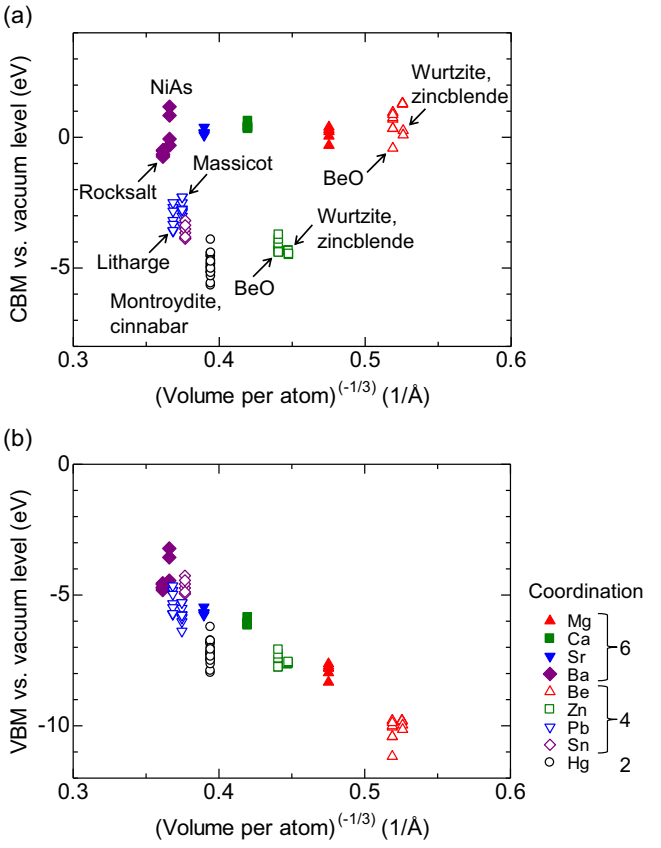

FIG. 11. (a) CBM and (b) VBM with respect to the vacuum level (the negatives of the EA and IP, respectively) plotted against the reciprocal of the cube root of volume per atom for stable and slightly metastable metal oxide polymorphs. The CBM and VBM refer to the values from nsc-dd hybrid functional calculations. Internal coordinates are relaxed during surface calculations. The prototype is identified when there are multiple prototypes for the same cation.

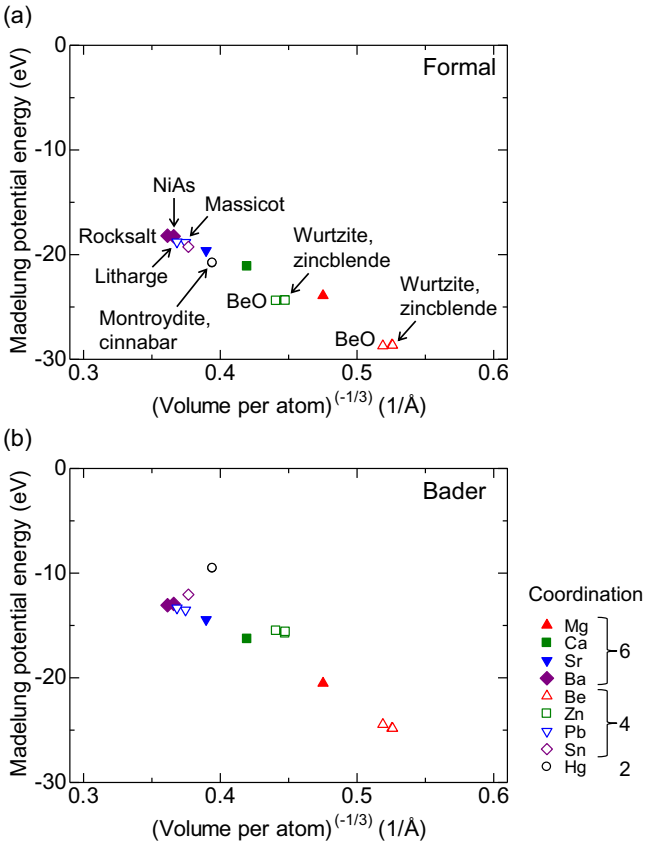

FIG. 12. Madelung potential energy for an electron at the O site vs the reciprocal of the cube root of volume per atom based on (a) formal and (b) Bader charges. The prototype is identified when there are multiple prototypes for the same cation.

(the negative of the IP) versus surface energy including IC relaxation. We see that the VBM (the negative of the IP) strongly depends on the cation species but is not closely correlated with the surface energy even within the same chemical composition. As in the prototypical surfaces, there is a general trend where the oxides composed of smaller cations such as Be, Mg, and Zn have lower VBMs (larger IPs) while those composed of larger cations, for instance Pb and Ba, have higher VBMs (smaller IPs). To clarify this point, Fig. 11 plots the VBM and CBM (the negatives of the IP and EA, respectively) versus the reciprocal of the cube root of volume per atom. The EA appears to have no direct correlation with the volume per atom [Fig. 11(a)]; by considering various cation species and crystal structures here, the tendency is much less clear than that of the prototypical rocksalt, zincblende, and wurtzite surfaces discussed above. This is reasonable since the states governing the CBM differ widely depending on the chemical composition. In contrast, there is a clear trend where the VBM moves downwards (the IP increases) with decreasing cation size [Fig. 11(b)]. The relation against $v^{1/3}$ is almost linear, which can be related to the nearly linear trend in the Madelung potential energy (Fig. 12, numerically calculated using the Ewald method as implemented in the PYMATGEN code) as in the cases of the prototypical rocksalt, zincblende, and wurtzite structures. The VBM (the negative of the IP) of HgO noticeably deviates from the trend, which could be attributed to its characteristic crystal structure. The coordination number of the Hg ions is 2 in both montroydite and cinnabar forms, although four more O ions are present at about 40% larger distances than the shortest Hg-O distance in both structures. This is in a stark contrast to the other oxides where the minimum coordination number is 4. Another feature of HgO is that its valence band consists of a significant hybridization of Hg $5d$, $6s$, $6p$, and O $2p$ states as discussed above. On the other hand, hybridization of the cation $3d$ and O $2p$ states occurs in ZnO, and that of the cation s, p, and O $2p$ states occurs in SnO and PbO. Since such hybridization is likely to raise the VBM as discussed above, hybridization by itself cannot explain the large downward deviation of HgO from the trend. Moreover, the VBMs (the negatives of the IPs) vary by roughly 2 eV for the same chemical composition, for instance in BeO, HgO, PbO, and BaO. For these oxides, the surface orientation dependence amounts to up to ∼1.7 eV within the same crystal structure. This variation is attributed to surface-specific characteristics rather than intrinsic bulk band structures.

Lastly, the effect of the atomic configuration at the surface is discussed using a high-pressure phase of BaO in the NiAs structure [118] as an example. Four surfaces shown in Fig. 13 are considered, which are $(10\bar{1}0)$, $(10\bar{1}2)$, $(10\bar{1}4)$, and $(2\bar{1}\bar{1}0)$.

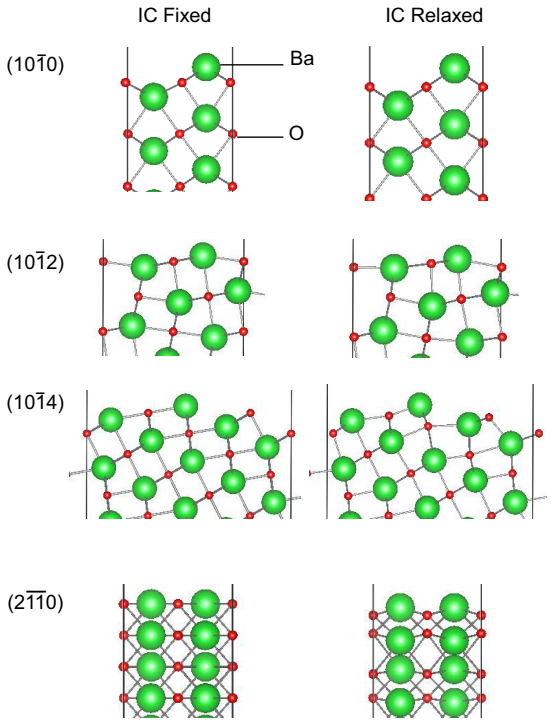

FIG. 13. Atomic structure of nonpolar surfaces of BaO with the NiAs structure before and after internal coordinate (IC) relaxation.

The (2$\bar{1}\bar{1}$0) surface is nonpolar type A (Tasker's type 1), while the others are nonpolar type B (Tasker's type 2) where the repeat unit consists of a Ba layer, an O layer, and another Ba layer. Table VI shows the VBM versus the vacuum level (the negative of the IP) with fixed and relaxed ICs during surface calculations. When ICs are fixed, the VBM (IP) for the (10$\bar{1}$0) surface is higher (the IP is smaller) by at least 1.8 eV compared to the other investigated surfaces because the anion and cation layers in the repeat unit are positioned far apart and the outermost layer is the cation layer (see previous discussion on Fig. 7). The IC relaxation changes the VBM (IP) only by ∼0.2 eV. The surfaces with large VBM (IP) differences of over 1 eV between fixed and relaxed IC calculations are (10$\bar{1}$4) and (2$\bar{1}\bar{1}$0). The surface energy changes most in the former, in terms of both absolute difference and the percentage in change, although atomic relaxation does not look significant in Fig. 13. The (2$\bar{1}\bar{1}$0) surface is the sole nonpolar type-A (Tasker's type-1) surface where there are both cations and anions in every layer prior to IC relaxation. Relaxation of ICs allows the cations to move closer to vacuum compared to the anions, resulting in a large increase in the VBM (decrease in the IP), as also found for surfaces of other crystal structures in Fig. 7. This relaxation, however, does not substantially reduce the surface energy as shown in Table VI. The resultant surface energies after atomic relaxation do not closely correlate with the VBM (IP) values, and such a trend is also observed in Fig. 10 for other materials. The chemical composition and volume more affect the VBM (IP), as can be found in Figs. 10 and 11 and discussed above.

TABLE VI. VBM versus the vacuum level (the negative of the IP) and surface energy for BaO with the NiAs structure when internal coordinates (ICs) are fixed and relaxed in surface calculations. The VBM and surface energy values are from nsc-dd hybrid functional and PBEsol(+U) calculations, respectively.

Surface	VBM vs vacuum (eV)			Surface energy (meV/Å^2)		
	IC fixed	IC relaxed	Difference	IC fixed	IC relaxed	Difference
(10$\bar{1}$0)	−3.03	−3.22	−0.19	51.9	39.5	−12.4
(10$\bar{1}$2)	−4.90	−4.70	0.20	50.3	36.9	−13.4
(10$\bar{1}$4)	−5.45	−4.45	1.00	102.0	55.4	−46.7
(2$\bar{1}\bar{1}$0)	−4.85	−3.60	1.25	68.7	41.5	−27.1

IV. CONCLUSIONS

The valence and conduction band positions with respect to the vacuum level, i.e., IPs and EAs, of nonpolar surfaces have been evaluated using PBEsol(+U) and nsc-dd hybrid functional calculations by taking binary oxides of formally closed-shell divalent cations as target systems. In particular, their dependence on the cation species, crystal structure, and surface orientation has been systematically investigated using an automatic slab model construction algorithm. As a result, the IPs are found to be related to the following factors: (1) cation size, which is represented by the cube root of volume per atom in this paper—a large cation size decreases the IP (increases the VBM with respect to the vacuum level) and the relation is almost linear, and the tendency is also recognized for the O 2s band center and O-site local potential with respect to the vacuum level, implying an electrostatic origin; (2) the presence or absence of significant cationic orbital contributions near the VBM; and (3) atomic relaxation near the surface. Factors 1 and 2 are associated with the cation species and the resultant bulk electronic structure. The effect of factor 3 mostly depends on the cation size and surface orientation, and amounts to up to ∼1 eV. The surface orientation dependence of the IP after IC relaxation within the same chemical composition and crystal structure is up to ∼1.7 eV in the systems considered. Nevertheless, factor 1, or lattice volume, is a determinant factor to the IPs. The EAs show a less clear tendency, which is attributed to the fact that the dominant orbital components vary with the cation species in the conduction bands.

ACKNOWLEDGMENTS

This work was supported by a Grant-in-Aid for Scientific Research (C) (Grant No. 18K04692) from Japan Society for the Promotion of Science and a Creation of Life Innovation Materials for Interdisciplinary and International Researcher Development project from Ministry of Education, Culture, Sports, Science and Technology, as well as the "Materials Research by Information Integration" Initiative (MI^{2}I) project of the Support Program for Starting Up Innovation Hub and CREST (Grants No. JPMJCR17J3 and No. JPMJCR17J2) from Japan Science and Technology Agency. Computing resources of ACCMS at Kyoto University and the Supercomputer Center in the Institute for Solid State Physics at the

University of Tokyo were used. The VESTA code [119] was used to draw Figs. 1, 8, 13, and 15.

APPENDIX: ALGORITHM TO DETECT IDENTICAL NONPOLAR TERMINATIONS

IPs and EAs are surface properties that depend on the orientation and termination of a surface, as mentioned above. First-principles calculations allow for explicit atomic level modeling of the surface, which is beneficial in estimating IPs and EAs of a given surface. On the flip side, one of the critical bottlenecks in the high-throughput calculations of surface properties is building appropriate slab-and-vacuum models when the surfaces are investigated on the basis of the supercell approach. This issue is relevant to the variation of the surface geometry associated with given crystal structures as well as the local modulation in atomic structure at the surfaces.

Tasker's categorization of surfaces into three distinct types [90] is widely used to classify the polarity of ionic compound surfaces. Layers of atoms in a Tasker's type-1 surface are neutral when formal charges are assumed, whereas those in a Tasker's type-2 surface are charged and arranged symmetrically such that there is no net dipole moment perpendicular to the surface plane. All layers in a Tasker's type-3 (polar) surface are charged and there is a perpendicular macroscopic dipole moment. On the other hand, Hinuma *et al.* redefined the polar surface and categorized nonpolar surfaces into three types based on a crystallographic approach [16]. A surface is nonpolar type A if the surface is not polar and each layer of atoms is stoichiometric. This is a stricter requirement than the Tasker's type-1 surface that could have charge neutrality based on the formal charge in every layer. Examples are the (100) SrO- and TiO_2-terminated surfaces of cubic perovskite $SrTiO_3$. These surfaces are not charge neutral and therefore are Tasker type 3 when actual net charges are considered. A surface is nonpolar type B if the boundaries of the dipole-free bulk unit cell [58] or, in other words, the repeat unit with no dipole moment perpendicular to the surface, lies between layers of atoms, and nonpolar type C if the boundaries must lie on layers of atoms. A nonpolar type C slab cannot, by definition, be simultaneously nonpolar and stoichiometric when simply cleaved from bulk though a nonpolar; however, a stoichiometric slab can be obtained by surface modification involving vacancies and/or adatoms. For example, the rocksalt (111) surface is Tasker type 3 (polar) but may become nonpolar type C because surface vacancy formation can yield a nonpolar and stoichiometric slab. The cubic perovskite (100) surface can also become nonpolar type C. Hinuma *et al.* provided an algorithm based on crystallography to obtain a nonpolar type A or B stoichiometric slab-and-vacuum model, if it exists, given the crystal, orientation, and minimum slab and vacuum thicknesses [16]. Their procedure automatically finds and evaluates the stoichiometry and polarity of four types of terminations, but they do not give an algorithm to identify identical terminations among the four.

Orientations/terminations of surfaces investigated in this paper are obtained by first identifying unique nonpolar surface orientations of a crystal. This is attained by exploiting information on crystal forms available in Table 3.2.3.2 of the International Tables of Crystallography A Edition 6 [120]. Orientations are equivalent when they belong to the same crystal form and nonpolar when orientation (hkl) is equivalent to $(\bar{h}\,\bar{k}\,\bar{l})$. Some orientations are nonpolar only when indices satisfy certain restrictions or, in other words, belong to a special crystal form in contrast to a general form. A choice of unique nonpolar orientations covering all space-group types is shown as Table VII.

The orientations for rhombohedral lattices in Table VII are based on the rhombohedral axes. Conversion between the rhombohedral orientation (h_r, k_r, l_r) and the hexagonal orientation (h_h, k_h, l_h) is performed by

$$\begin{pmatrix} h_r \\ k_r \\ l_r \end{pmatrix} = \begin{pmatrix} 2 & 1 & 1 \\ \bar{1} & 1 & 1 \\ \bar{1} & \bar{2} & 1 \end{pmatrix} \begin{pmatrix} h_h \\ k_h \\ l_h \end{pmatrix}$$

or

$$\begin{pmatrix} h_h \\ k_h \\ l_h \end{pmatrix} = \begin{pmatrix} 1 & \bar{1} & 0 \\ 0 & 1 & \bar{1} \\ 1 & 1 & 1 \end{pmatrix} \begin{pmatrix} h_r \\ k_r \\ l_r \end{pmatrix}$$

and then dividing by a positive integer to make the orientation coprime.

To generate slab-and-vacuum models, a sufficiently large set of orientations (hkl) is obtained where h is not negative ($h \geqslant 0$), at least one element of the set [121] is positive (>0), and nonzero elements of the set $\{|h|, |k|, |l|\}$ are coprime (if there is only one nonzero element, that element is set to 1). The *conventional unit cell*, as defined according to Ref. [122], is taken as the starting point and can be obtained using, for instance, the SPGLIB code [123]. Its basis vectors are denoted as $(\mathbf{a}, \mathbf{b}, \mathbf{c})$. Defining in-plane vectors $h'\mathbf{a} + k'\mathbf{b} + l'\mathbf{c}$ as vectors that satisfy $(h', k', l') \cdot (h, k, l)^{\mathrm{T}} = 0$, the (hkl) *primitive cell* has basis vectors $(\mathbf{a}_{\mathrm{P}}, \mathbf{b}_{\mathrm{P}}, \mathbf{c}_{1\mathrm{P}})$ where $\mathbf{a}_{\mathrm{P}}$ and $\mathbf{b}_{\mathrm{P}}$ are in-plane vectors. The *unit layer thickness* $z_{1\mathrm{u}}$ is the minimum $z_{1\mathrm{u}}$ where a slab constructed from the (hkl) primitive cell with boundaries z' and $z' + z_{1\mathrm{u}}$ is the same as one with boundaries $z' + z_{1\mathrm{u}}$ and $z' + 2z_{1\mathrm{u}}$. If a nonpolar slab can be taken, there is exactly one z_{Pc} in the range $0 \leqslant z_{\mathrm{Pc}} < 1/2$ based on the (hkl) primitive cell where an isometry, or symmetry operation that maps a crystal onto itself, maps atoms in the range $z < z_{\mathrm{Pc}}$ to $z > z_{\mathrm{Pc}}$ and vice versa. This z_{Pc} is defined as the *unique potential slab center*. The polarity type of a nonpolar orientation can be investigated using the (hkl) 3-supercell, which is a $1 \times 1 \times 3$ supercell of the (hkl) primitive cell. The 3-index notation is used here even for hexagonal crystals such that the same procedure can be applied to all crystals. Four terminations I to IV are defined, and slabs are prepared by removing atoms with the z coordinate outside the ranges defined in Table VIII from the (hkl) 3-supercell. These terminations are also shown in Fig. 14, alongside four ranges A–D defined in Table IX. One unit layer contains two distinct potential slab centers by definition, and two slabs, one with integer and another with half-integer thickness of the unit layer thickness, are considered for each potential slab center. Use of the $1 \times 1 \times 3$ supercell and choice of ranges defined in Table VIII ensure that each range is wider than one repeat unit, hence there must be some atoms in the range, and the

TABLE VII. List of unique nonpolar orientations. Indices h, k, and l must satisfy the following: at least one element of the set $\{h, k, l\}$ is positive (>0), and nonzero elements of the set $\{|h|, |k|, |l|\}$ are coprime (if there is only one nonzero element, that element must be 1).

Point group	Space group number	Nonpolar orientation	Restriction
1	1	None	Never nonpolar
$\bar{1}$	2	(hkl)	$h > 0$
		$(0kl)$	$k \geqslant 0$
2	3–5	$(h0l)$	$h \geqslant 0$
m	6–9	(010)	
2/m	10–15	(hkl)	$h \geqslant 0, k \geqslant 0$
222	16–24	$(hk0)$	$h \geqslant 0, k > 0$
		$(h0l)$	$h > 0, l \geqslant 0$
		$(0kl)$	$k \geqslant 0, l > 0$
$mm2$	25–46	$(hk0)$	$h \geqslant 0, k \geqslant 0$
mmm	47–74	(hkl)	$h \geqslant 0, k \geqslant 0, l \geqslant 0$
4	75–80	$(hk0)$	$h \geqslant 0, k > 0$
$\bar{4}$	81–82	$(hk0)$	$h \geqslant 0, k > 0$
		(001)	
4/m	83–88	(hkl)	$h \geqslant 0, k > 0, l \geqslant 0$
		(001)	
422	89–98	$(hk0)$	$0 < k \leqslant h$
		$(h0l)$	$h > 0, l \geqslant 0$
		(hhl)	$h \geqslant 0, l > 0$
4mm	99–110	$(hk0)$	$0 \leqslant k \leqslant h$
$\bar{4}2m$	111–114, 121–122	$(hk0)$	$0 \leqslant k \leqslant h$
		$(h0l)$	$h \geqslant 0, l > 0$
$\bar{4}m2$	115–120	$(hk0)$	$0 \leqslant k \leqslant h$
		(hhl)	$h \geqslant 0, l > 0$
4/mmm	123–142	(hkl)	$0 \leqslant k \leqslant h, l \geqslant 0$
3 (hP, hR)	143–146	None	Never nonpolar
$\bar{3}$ (hP)	147	(hkl)	$h \geqslant 0, k \geqslant 0$
$\bar{3}$ (hR)	148	(hkl)	$l < h, l < k, h > 0, k > 0, h \neq k$
		(hhl)	$h > 0, l \neq 0$
		$(hk0)$	$h \geqslant 0$
312 (hP), 32 (hR)	149, 151, 153, 155	(hhl)	$h \geqslant 0$
321 (hP)	150, 152, 154	$(h0l)$	$h \geqslant 0$
3m1 (hP)	156, 158	(110)	
31m (hP)	157, 159	(100)	
3m (hR)	160–161	$(10\bar{1})$	
$\bar{3}$1m (hP)	162–163	(hkl)	$0 < k \leqslant h$
		$(h0l)$	$h \geqslant 0, l \geqslant 0$
$\bar{3}$1m (hP)	164–165	(hkl)	$0 \leqslant k < h$
		(hhl)	$h \geqslant 0, l \geqslant 0$
$\bar{3}m$ (hR)	166–167	(hkl)	$l \leqslant k \leqslant h, k > 0, l \neq 0$
		$(hk0)$	$0 \leqslant \lvert k \rvert \leqslant h$
6	168–173	$(hk0)$	$h > 0, k \geqslant 0$
$\bar{6}$	174	(001)	
6/m	175, 176	(hkl)	$h > 0, k \geqslant 0, l \geqslant 0$
		(001)	
622	177–182	$(hk0)$	$0 < k \leqslant h$
		$(h0l)$	$h > 0, l \geqslant 0$
		(hhl)	$h \geqslant 0, l > 0$
6mm	183–186	$(hk0)$	$0 \leqslant k \leqslant h$
$\bar{6}m2$	187, 188	(hhl)	$h \geqslant 0, l \geqslant 0$
$\bar{6}2m$	189, 190	$(h0l)$	$h \geqslant 0, l \geqslant 0$
6/mmm	191–194	(hkl)	$0 \leqslant k \leqslant h, l \geqslant 0$
23	195–199	$(hk0)$	$h \geqslant 0, k \geqslant 0$
$m\bar{3}$	200–206	(hkl)	$0 \leqslant l < h, l < k, h \neq k$
		(hhl)	$h \geqslant 0, l \geqslant 0$
432	207–214	(hhl)	$h \geqslant 0, l \geqslant 0$
		$(hk0)$	$0 < k < h$
$\bar{4}3m$	215–220	$(hk0)$	$0 \leqslant k \leqslant h$
$m\bar{3}m$	221–230	(hkl)	$0 \leqslant l \leqslant k \leqslant h$

TABLE VIII. Ranges of z coordinates that correspond to different terminations in an (hkl) 3-supercell. z_{Pc} and $z_{1\mathrm{u}}$ are the unique potential slab center and unit layer thickness determined in an (hkl) primitive cell, respectively. The (hkl) 3-supercell is a $1 \times 1 \times 3$ supercell of the (hkl) primitive cell.

Termination	Range of z
I	$(z_{\mathrm{Pc}} - z_{1\mathrm{u}}/4 + 1)/3 \leqslant z \leqslant (z_{\mathrm{Pc}} + 5z_{1\mathrm{u}}/4 + 1)/3$
II	$(z_{\mathrm{Pc}} - 3z_{1\mathrm{u}}/4 + 1)/3 \leqslant z \leqslant (z_{\mathrm{Pc}} + 3z_{1\mathrm{u}}/4 + 1)/3$
III	$(z_{\mathrm{Pc}} - 2z_{1\mathrm{u}}/4 + 1)/3 \leqslant z \leqslant (z_{\mathrm{Pc}} + 2z_{1\mathrm{u}}/4 + 1)/3$
IV	$(z_{\mathrm{Pc}} + 1)/3 \leqslant z \leqslant (z_{\mathrm{Pc}} + 4z_{1\mathrm{u}}/4 + 1)/3$

z coordinate of the range is entirely in the range $0 < z < 1$. Two considered terminations are equivalent when there are no atoms in the given corresponding range because the resulting slab contains the same number of atoms. For instance, terminations I and III are equivalent if there are no atoms in range A. The four terminations I–IV become identical if there are no atoms in $(z_{\mathrm{Pc}} + z_{1\mathrm{u}}/4 + 1)/3 \leqslant z \leqslant (z_{\mathrm{Pc}} + 3z_{1\mathrm{u}}/4 + 1)/3$ (includes both ranges A and B) or if there are no atoms in $(z_{\mathrm{Pc}} - z_{1\mathrm{u}}/4 + 1)/3 \leqslant z \leqslant (z_{\mathrm{Pc}} + z_{1\mathrm{u}}/4 + 1)/3$ (includes both ranges C and D). The terminations I to IV are defined with nonstrict inequalities on both sides as atoms can exist on the boundaries. In fact, atoms in a nonstoichiometric composition exist on both boundaries in all nonpolar type-C surfaces. Such a slab is indeed nonpolar but is not stoichiometric, and some form of reconstruction is necessary to make a nonpolar and stoichiometric slab. Choosing only one boundary results in a polar slab unless there are no atoms on the boundary.

The wurtzite ZnO $(10\bar{1}0)$ surface is used as an example to demonstrate identification of duplicate terminations. Figure 15(a) shows the (100) primitive cell of ZnO. Both Zn and O occupy $2b$ sites. Here, $z_{\mathrm{Pc}} = 0$ (symmetry ensured by the twofold screw axes at this z coordinate) and $z_{1\mathrm{u}} = 1$. Figure 15(b) gives the (100) 3-supercell. Ranges for terminations I to IV are shown using blue arrows in the figure,

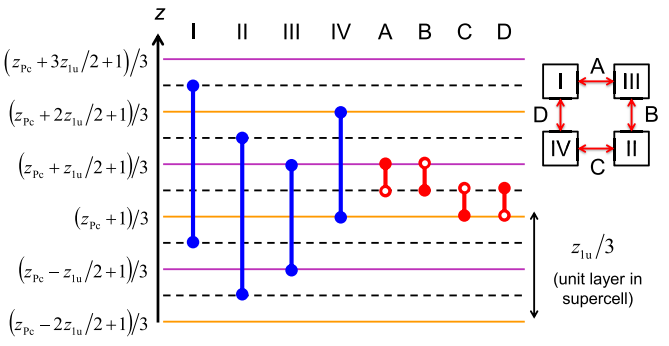

FIG. 14. Range of z coordinates that define four terminations I-IV in an (hkl) 3-supercell and ranges A–D used to identify identical terminations. Filled and empty circles indicate that the boundary is included and excluded, respectively. The purple and orange lines indicate the positions of two different potential slab centers, while dashed lines position exactly between purple and orange lines. z_{Pc} and $z_{1\mathrm{u}}$ are the unique potential slab center and unit layer thickness determined in an (hkl) primitive cell, respectively. The (hkl) 3-supercell is a $1 \times 1 \times 3$ supercell of the (hkl) primitive cell.

TABLE IX. Four ranges of z coordinates in an (hkl) 3-supercell and equivalent terminations if there are no atoms in the corresponding range. z_{Pc} and $z_{1\mathrm{u}}$ are the unique potential slab center and unit layer thickness determined in an (hkl) primitive cell, respectively. The (hkl) 3-supercell is a $1 \times 1 \times 3$ supercell of the (hkl) primitive cell.

Range	Range of z	Equivalent terminations
A	$(z_{\mathrm{Pc}} + z_{1\mathrm{u}}/4 + 1)/3 < z \leqslant (z_{\mathrm{Pc}} + 2z_{1\mathrm{u}}/4 + 1)/3$	I, III
B	$(z_{\mathrm{Pc}} + z_{1\mathrm{u}}/4 + 1)/3 \leqslant z < (z_{\mathrm{Pc}} + 2z_{1\mathrm{u}}/4 + 1)/3$	II, III
C	$(z_{\mathrm{Pc}} + 1)/3 \leqslant z < (z_{\mathrm{Pc}} + z_{1\mathrm{u}}/4 + 1)/3$	II, IV
D	$(z_{\mathrm{Pc}} + 1)/3 < z \leqslant (z_{\mathrm{Pc}} + z_{1\mathrm{u}}/4 + 1)/3$	I, IV

and ranges A to D are indicated by red arrows. Ranges A and B differ by which end point is included, and the same holds for C and D. There are atoms in ranges A and B but not in C and D, which means that terminations I, II, and IV are equivalent and distinct from termination III. There are two distinct gaps between layers of atoms in Fig. 15(b). The slab is obtained by cleaving at the wide and narrow gaps for the former and latter type of termination, respectively. Actual first-principles calculations could be conducted after choosing the out-of-plane basis vector with minimum length arranged from the algorithm by Semaev [124]. We define the basis

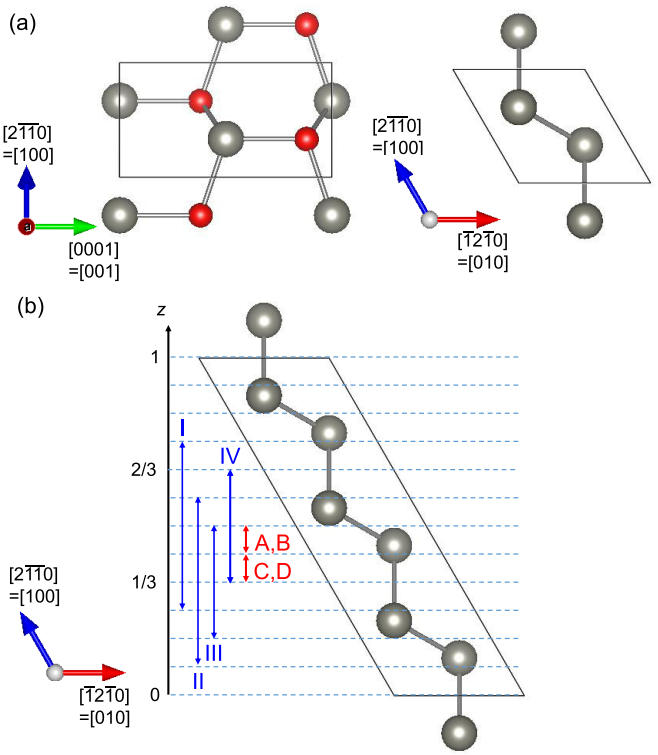

FIG. 15. (a) Two views of the (100) primitive cell of wurtzite ZnO. (b) The (100) 3-supercell of ZnO and various slab ranges given in Fig. 14. The gray and red circles represent Zn and O atoms, respectively, and the frames indicate the (100) primitive cell and (100) 3-supercell in (a) and (b), respectively.

vectors of the (hkl) n supercell as $(\mathbf{a}_P, \mathbf{b}_P, \mathbf{c}_{nP})$, which is a $1 \times 1 \times n$ supercell of the (hkl) primitive cell. Two quantities

$$y_1 = -\frac{\frac{(\mathbf{a}_P \cdot \mathbf{c}_{nP})}{|\mathbf{a}_P|^2} - \frac{(\mathbf{a}_P \cdot \mathbf{b}_P)(\mathbf{b}_P \cdot \mathbf{c}_{nP})}{|\mathbf{a}_P|^2 |\mathbf{b}_P|^2}}{1 - \frac{(\mathbf{a}_P \cdot \mathbf{b}_P)^2}{|\mathbf{a}_P|^2 |\mathbf{b}_P|^2}}, \tag{A1}$$

$$y_2 = -\frac{\frac{(\mathbf{b}_P \cdot \mathbf{c}_{nP})}{|\mathbf{b}_P|^2} - \frac{(\mathbf{a}_P \cdot \mathbf{b}_P)(\mathbf{a}_P \cdot \mathbf{c}_{nP})}{|\mathbf{a}_P|^2 |\mathbf{b}_P|^2}}{1 - \frac{(\mathbf{a}_P \cdot \mathbf{b}_P)^2}{|\mathbf{a}_P|^2 |\mathbf{b}_P|^2}} \tag{A2}$$

are calculated together with four integers $y_{1+} = \lceil y_1 \rceil$, $y_{1-} = \lfloor y_1 \rfloor$, $y_{2+} = \lceil y_2 \rceil$, and $y_{2-} = \lfloor y_2 \rfloor$. Here, $\lceil\ \rceil$ and $\lfloor\ \rfloor$ are ceiling and floor functions, respectively. Norms of four vectors are obtained as

$$n_{++} = |\mathbf{c}_{nP} + y_{1+}\mathbf{a}_P + y_{2+}\mathbf{b}_P|, \tag{A3}$$

$$n_{+-} = |\mathbf{c}_{nP} + y_{1+}\mathbf{a}_P + y_{2-}\mathbf{b}_P|, \tag{A4}$$

$$n_{-+} = |\mathbf{c}_{nP} + y_{1-}\mathbf{a}_P + y_{2+}\mathbf{b}_P|, \tag{A5}$$

$$n_{--} = |\mathbf{c}_{nP} + y_{1-}\mathbf{a}_P + y_{2-}\mathbf{b}_P|. \tag{A6}$$

The vector with the smallest norm is chosen as the out-of-plane basis vector.

In many cases there are a large number of nonpolar orientations. For instance, there is at least one nonpolar termination for all orientations when there is inversion symmetry, aside from the stoichiometry of the slab. Therefore, a limit must be imposed on the number of orientations to be investigated. This paper considered nonpolar A or B orientations with sixth smallest in-plane area or larger and orientations with in-plane area exceeding five times the smallest nonpolar orientation are removed from consideration. Here, the in-plane area is the minimum nonzero area of the slab spanned by two in-plane vectors. The number of orientations that need to be considered depends on the system. The stable (100) surface of the rocksalt structure has the smallest in-plane area among nonpolar A and B surfaces. However, the most stable surface does not necessarily have a small in-plane area. As an example, the $(11\bar{1})$ surface is most stable followed by (111) in monoclinic ZrO_2 with the baddeleyite structure [125]. These orientations have the ninth and tenth smallest in-plane area, respectively, and the in-plane area is 1.65 and 1.85 times larger than the smallest orientation, which is (001). This indicates that low symmetry structures could require sampling of a large number of orientations with relatively similar small in-plane area.

[1] D. Cahen and A. Kahn, Adv. Mater. **15**, 271 (2003).
[2] H. Hosono, *Transparent Electronics: From Synthesis to Applications* (Wiley, New York, 2010).
[3] A. Franciosi and C. G. Van de Walle, Surf. Sci. Rep. **25**, 1 (1996).
[4] J. Robertson, J. Vac. Sci. Technol. A **31**, 050821 (2013).
[5] H. Ehrenreich and D. Turnbull, in *Solid State Physics*, edited by E. Henry and T. David (Academic, Boston, 1992), p. 1.
[6] Y. Ping, D. Rocca, and G. Galli, Chem. Soc. Rev. **42**, 2437 (2013).
[7] Y. Kumagai, K. T. Butler, A. Walsh, and F. Oba, Phys. Rev. B **95**, 125309 (2017).
[8] Y. Hinuma, A. Grüneis, G. Kresse, and F. Oba, Phys. Rev. B **90**, 155405 (2014).
[9] Y. Hinuma, F. Oba, Y. Kumagai, and I. Tanaka, Phys. Rev. B **88**, 035305 (2013).
[10] Y. Hinuma, F. Oba, Y. Nose, and I. Tanaka, J. Appl. Phys. **114**, 043718 (2013).
[11] S. P. Ong, W. D. Richards, A. Jain, G. Hautier, M. Kocher, S. Cholia, D. Gunter, V. L. Chevrier, K. A. Persson, and G. Ceder, Comp. Mater. Sci. **68**, 314 (2013).
[12] S. P. Ong, S. Cholia, A. Jain, M. Brafman, D. Gunter, G. Ceder, and K. A. Persson, Comp. Mater. Sci. **97**, 209 (2015).
[13] R. H. Taylor, F. Rose, C. Toher, O. Levy, K. Yang, M. Buongiorno Nardelli, and S. Curtarolo, Comp. Mater. Sci. **93**, 178 (2014).
[14] Y. Kumagai and F. Oba, Phys. Rev. B **89**, 195205 (2014).
[15] Y. Hinuma, G. Pizzi, Y. Kumagai, F. Oba, and I. Tanaka, Comp. Mater. Sci. **128**, 140 (2017).
[16] Y. Hinuma, Y. Kumagai, F. Oba, and I. Tanaka, Comp. Mater. Sci. **113**, 221 (2016).
[17] G. Pizzi, A. Cepellotti, R. Sabatini, N. Marzari, and B. Kozinsky, Comp. Mater. Sci. **111**, 218 (2016).
[18] J. E. Saal, S. Kirklin, M. Aykol, B. Meredig, and C. Wolverton, JOM **65**, 1501 (2013).
[19] F. Oba and Y. Kumagai, Appl. Phys. Express **11**, 060101 (2018).
[20] S. Curtarolo, G. L. W. Hart, M. B. Nardelli, N. Mingo, S. Sanvito, and O. Levy, Nat. Mater. **12**, 191 (2013).
[21] L. M. Ghiringhelli, C. Carbogno, S. Levchenko, F. Mohamed, G. Huhs, M. Lüders, M. Oliveira, and M. Scheffler, NPJ Comput. Mater. **3**, 46 (2017).
[22] P. Hohenberg and W. Kohn, Phys. Rev. **136**, B864 (1964).
[23] W. Kohn and L. J. Sham, Phys. Rev. **140**, A1133 (1965).
[24] A. Jain, S. P. Ong, G. Hautier, W. Chen, W. D. Richards, S. Dacek, S. Cholia, D. Gunter, D. Skinner, G. Ceder, and K. A. Persson, APL Mater. **1**, 011002 (2013).
[25] S. Curtarolo, W. Setyawan, S. Wang, J. Xue, K. Yang, R. H. Taylor, L. J. Nelson, G. L. W. Hart, S. Sanvito, M. Buongiorno-Nardelli, N. Mingo, and O. Levy, Comp. Mater. Sci. **58**, 227 (2012).
[26] S. Kirklin, J. E. Saal, B. Meredig, A. Thompson, J. W. Doak, M. Aykol, S. Rühl, and C. Wolverton, NPJ Comput. Mater. **1**, 15010 (2015).
[27] A. Zakutayev, X. Zhang, A. Nagaraja, L. Yu, S. Lany, T. O. Mason, D. S. Ginley, and A. Zunger, J. Am. Chem. Soc. **135**, 10048 (2013).
[28] Y. Wu, P. Lazic, G. Hautier, K. Persson, and G. Ceder, Energy Environ. Sci. **6**, 157 (2013).
[29] R. Gautier, X. Zhang, L. Hu, L. Yu, Y. Lin, O. L. SundeTor, D. Chon, K. R. Poeppelmeier, and A. Zunger, Nat. Chem. **7**, 308 (2015).

[30] W. Chen, J.-H. Pohls, G. Hautier, D. Broberg, S. Bajaj, U. Aydemir, Z. M. Gibbs, H. Zhu, M. Asta, G. J. Snyder, B. Meredig, M. A. White, K. Persson, and A. Jain, J. Mater. Chem. C **4**, 4414 (2016).

[31] Y. Hinuma, T. Hatakeyama, Y. Kumagai, L. A. Burton, H. Sato, Y. Muraba, S. Iimura, H. Hiramatsu, I. Tanaka, H. Hosono, and F. Oba, Nat. Commun. **7**, 11962 (2016).

[32] K. T. Butler, J. M. Frost, J. M. Skelton, K. L. Svane, and A. Walsh, Chem. Soc. Rev. **45**, 6138 (2016).

[33] A. Jain, G. Hautier, S. P. Ong, and K. Persson, J. Mater. Res. **31**, 977 (2016).

[34] W. Sun, S. T. Dacek, S. P. Ong, G. Hautier, A. Jain, W. D. Richards, A. C. Gamst, K. A. Persson, and G. Ceder, Sci. Adv. **2**, e1600225 (2016).

[35] L. Ward, A. Agrawal, A. Choudhary, and C. Wolverton, NPJ Comput. Mater. **2**, 16028 (2016).

[36] G. Hautier, A. Miglio, G. Ceder, G.-M. Rignanese, and X. Gonze, Nat. Commun. **4**, 2292 (2013).

[37] N. Sarmadian, R. Saniz, B. Partoens, D. Lamoen, K. Volety, G. Huyberechts, and J. Paul, PCCP **16**, 17724 (2014).

[38] I. E. Castelli, T. Olsen, S. Datta, D. D. Landis, S. Dahl, K. S. Thygesen, and K. W. Jacobsen, Energy Environ. Sci. **5**, 5814 (2012).

[39] A. A. Emery, J. E. Saal, S. Kirklin, V. I. Hegde, and C. Wolverton, Chem. Mater. **28**, 5621 (2016).

[40] H. Hayashi, S. Katayama, T. Komura, Y. Hinuma, T. Yokoyama, K. Mibu, F. Oba, and I. Tanaka, Adv. Sci. **4**, 1600246 (2017).

[41] K. Yim, Y. Yong, J. Lee, K. Lee, H.-H. Nahm, J. Yoo, C. Lee, C. Seong Hwang, and S. Han, NPG Asia Mater. **7**, e190 (2015).

[42] I. E. Castelli, F. Hüser, M. Pandey, H. Li, K. S. Thygesen, B. Seger, A. Jain, K. A. Persson, G. Ceder, and K. W. Jacobsen, Adv. Energy Mater. **5**, 1400915 (2015).

[43] J. Lee, A. Seko, K. Shitara, K. Nakayama, and I. Tanaka, Phys. Rev. B **93**, 115104 (2016).

[44] O. Isayev, C. Oses, C. Toher, E. Gossett, S. Curtarolo, and A. Tropsha, Nat. Commun. **8**, 15679 (2017).

[45] K. Hashimoto, H. Irie, and A. Fujishima, Jpn. J. Appl. Phys. **44**, 8269 (2005).

[46] Y.-M. Chiang, D. P. Birnie, and W. D. Kingery, *Physical Ceramics: Principles for Ceramic Science and Engineering,* MIT Series in Materials Science and Engineering (Wiley, New York, 1997).

[47] C. N. R. Rao and B. Raveau, *Transition Metal Oxides: Structure, Properties, and Synthesis of Ceramic Oxides* (Wiley, New York, 1998).

[48] P. A. Cox, *Transition Metal Oxides: An Introduction to Their Electronic Structure and Properties,* International Series of Monographs on Chemistry Vol. 27 (Clarendon, Oxford, 1992).

[49] V. E. Henrich and P. A. Cox, *The Surface Science of Metal Oxides* (Cambridge, Cambridge, England, 1996).

[50] H. Hosono, K. Hayashi, T. Kamiya, T. Atou, and T. Susaki, Sci. Technol. Adv. Mater. **12**, 034303 (2011).

[51] E. Fortunato, P. Barquinha, and R. Martins, Adv. Mater. **24**, 2945 (2012).

[52] M. Lorenz, M. S. R. Rao, T. Venkatesan, E. Fortunato, P. Barquinha, R. Branquinho, D. Salgueiro, R. Martins, E. Carlos, A. Liu, F. K. Shan, M. Grundmann, H. Boschker, J. Mukherjee, M. Priyadarshini, N. DasGupta, D. J. Rogers, F. H. Teherani, E. V. Sandana, P. Bove, K. Rietwyk, A. Zaban, A. Veziridis, A. Weidenkaff, M. Muralidhar, M. Murakami, S. Abel, J. Fompeyrine, J. Zuniga-Perez, R. Ramesh, N. A. Spaldin, S. Ostanin, V. Borisov, I. Mertig, V. Lazenka, G. Srinivasan, W. Prellier, M. Uchida, M. Kawasaki, R. Pentcheva, P. Gegenwart, F. M. Granozio, J. Fontcuberta, and N. Pryds, J. Phys. D **49**, 433001 (2016).

[53] S. D. Ha and S. Ramanathan, J. Appl. Phys. **110**, 071101 (2011).

[54] N. K. Elumalai, C. Vijila, R. Jose, A. Uddin, and S. Ramakrishna, Mater. Renew. Sustain. Energy **4**, 11 (2015).

[55] S. J. A. Moniz, S. A. Shevlin, D. J. Martin, Z.-X. Guo, and J. Tang, Energy Environ. Sci. **8**, 731 (2015).

[56] ICSD database, https://icsd.fiz-karlsruhe.de/search/.

[57] Y. Hinuma, H. Hayashi, Y. Kumagai, I. Tanaka, and F. Oba, Phys. Rev. B **96**, 094102 (2017).

[58] J. Goniakowski, F. Finocchi, and C. Noguera, Rep. Prog. Phys. **71**, 016501 (2008).

[59] J. P. Perdew, A. Ruzsinszky, G. I. Csonka, O. A. Vydrov, G. E. Scuseria, L. A. Constantin, X. Zhou, and K. Burke, Phys. Rev. Lett. **100**, 136406 (2008).

[60] V. I. Anisimov, J. Zaanen, and O. K. Andersen, Phys. Rev. B **44**, 943 (1991).

[61] S. L. Dudarev, G. A. Botton, S. Y. Savrasov, C. J. Humphreys, and A. P. Sutton, Phys. Rev. B **57**, 1505 (1998).

[62] T. Shimazaki and Y. Asai, Chem. Phys. Lett. **466**, 91 (2008).

[63] M. A. L. Marques, J. Vidal, M. J. T. Oliveira, L. Reining, and S. Botti, Phys. Rev. B **83**, 035119 (2011).

[64] D. Koller, P. Blaha, and F. Tran, J. Phys.: Condens. Matter **25**, 435503 (2013).

[65] M. Gerosa, C. E. Bottani, L. Caramella, G. Onida, C. Di Valentin, and G. Pacchioni, Phys. Rev. B **91**, 155201 (2015).

[66] J. H. Skone, M. Govoni, and G. Galli, Phys. Rev. B **89**, 195112 (2014).

[67] T. Shimazaki and T. Nakajima, J. Chem. Phys. **141**, 114109 (2014).

[68] J. H. Skone, M. Govoni, and G. Galli, Phys. Rev. B **93**, 235106 (2016).

[69] M. Gerosa, C. E. Bottani, C. D. Valentin, G. Onida, and G. Pacchioni, J. Phys.: Condens. Matter **30**, 044003 (2018).

[70] W. Chen, G. Miceli, G.-M. Rignanese, and A. Pasquarello, Phys. Rev. Mater. **2**, 073803 (2018).

[71] L. Hedin, Phys. Rev. **139**, A796 (1965).

[72] M. S. Hybertsen and S. G. Louie, Phys. Rev. B **34**, 5390 (1986).

[73] Y. Hinuma, Y. Kumagai, I. Tanaka, and F. Oba, Phys. Rev. B **95**, 075302 (2017).

[74] Y. Kumagai, N. Tsunoda, and F. Oba, Phys. Rev. Appl. **9**, 034019 (2018).

[75] P. G. Moses, M. Miao, Q. Yan, and C. G. Van de Walle, J. Chem. Phys. **134**, 084703 (2011).

[76] A. Grüneis, G. Kresse, Y. Hinuma, and F. Oba, Phys. Rev. Lett. **112**, 096401 (2014).

[77] A. Alkauskas and A. Pasquarello, Physica B: Condensed Matter **401-402**, 670 (2007).

[78] F. Tran, Phys. Lett. A **376**, 879 (2012).

[79] P. E. Blöchl, Phys. Rev. B **50**, 17953 (1994).

[80] G. Kresse and J. Furthmüller, Phys. Rev. B **54**, 11169 (1996).

[81] G. Kresse and D. Joubert, Phys. Rev. B **59**, 1758 (1999).

[82] J. P. Perdew, K. Burke, and M. Ernzerhof, Phys. Rev. Lett. **77**, 3865 (1996).

[83] J. Sun, A. Ruzsinszky, and J. P. Perdew, Phys. Rev. Lett. **115**, 036402 (2015).

[84] A. Janotti, D. Segev, and C. G. Van de Walle, Phys. Rev. B **74**, 045202 (2006).

[85] F. Oba, M. Choi, A. Togo, and I. Tanaka, Sci. Technol. Adv. Mater. **12**, 034302 (2011).

[86] G. Henkelman, A. Arnaldsson, and H. Jónsson, Comp. Mater. Sci. **36**, 354 (2006).

[87] E. Sanville., S. D. Kenny, R. Smith, and G. Henkelman, J. Comput. Chem. **28**, 899 (2007).

[88] W. Tang, E. Sanville, and G. Henkelman, J. Phys.: Condens. Matter **21**, 084204 (2009).

[89] M. Yu and D. R. Trinkle, J. Chem. Phys. **134**, 064111 (2011).

[90] P. W. Tasker, J. Phys. C **12**, 4977 (1979).

[91] Y. Hinuma, F. Oba, Y. Kumagai, and I. Tanaka, Phys. Rev. B **86**, 245433 (2012).

[92] S. Baroni and R. Resta, Phys. Rev. B **33**, 7017 (1986).

[93] M. Gajdoš, K. Hummer, G. Kresse, J. Furthmüller, and F. Bechstedt, Phys. Rev. B **73**, 045112 (2006).

[94] S. Adachi,*The Handbook on Optical Constants of Semiconductors: In Tables and Figures* (World Scientific, Singapore, 2012).

[95] I. M. Boswarva, Phys. Rev. B **1**, 1698 (1970).

[96] J. Heyd, G. Scuseria, and M. Ernzerhof, J. Chem. Phys. **118**, 8207 (2003).

[97] J. Heyd, G. E. Scuseria, and M. Ernzerhof, J. Chem. Phys. **124**, 219906 (2006).

[98] A. V. Krukau, O. A. Vydrov, A. F. Izmaylov, and G. E. Scuseria, J. Chem. Phys. **125**, 224106 (2006).

[99] J. Perdew, M. Ernzerhof, and K. Burke, J. Chem. Phys. **105**, 9982 (1996).

[100] C. Adamo and V. Barone, J. Chem. Phys. **110**, 6158 (1999).

[101] M. Ernzerhof and G. Scuseria, J. Chem. Phys. **110**, 5029 (1999).

[102] J. A. McLeod, R. G. Wilks, N. A. Skorikov, L. D. Finkelstein, M. Abu-Samak, E. Z. Kurmaev, and A. Moewes, Phys. Rev. B **81**, 245123 (2010).

[103] A. V. Emeline, G. V. Kataeva, V. K. Ryabchuk, and N. Serpone, J. Phys. Chem. B **103**, 9190 (1999).

[104] R. C. Whited, C. J. Flaten, and W. C. Walker, Solid State Commun. **13**, 1903 (1973).

[105] A. S. Rao and R. J. Kearney, Phys. Status Solidi B **95**, 243 (1979).

[106] M. Yasir, J. Dahl, M. Kuzmin, J. Lång, M. Tuominen, M. P. J. Punkkinen, P. Laukkanen, K. Kokko, V. M. Korpijärvi, V. Polojärvi, and M. Guina, Appl. Phys. Lett. **103**, 191601 (2013).

[107] D. C. Reynolds, D. C. Look, B. Jogai, C. W. Litton, G. Cantwell, and W. C. Harsch, Phys. Rev. B **60**, 2340 (1999).

[108] O. Madelung, *Semiconductors: Data Handbook* (Springer-Verlag, Berlin, 2004).

[109] H. Hosono, Y. Ogo, H. Yanagi, and T. Kamiya, Electrochem. Solid-State Lett. **14**, H13 (2011).

[110] A. Qamar, K. LeBlanc, O. Semeniuk, A. Reznik, J. Lin, Y. Pan, and A. Moewes, Sci. Rep. **7**, 13159 (2017).

[111] S. Radhakrishnan, M. N. Kamalasanan, and P. C. Mehendru, J. Mater. Sci. **18**, 1912 (1983).

[112] T. Jaouen, G. Jézéquel, G. Delhaye, B. Lépine, P. Turban, and P. Schieffer, Appl. Phys. Lett. **97**, 232104 (2010).

[113] W. Mönch, in *Semiconductor Surfaces and Interfaces* (Springer, Berlin, 2001).

[114] K. Jacobi, G. Zwicker, and A. Gutmann, Surf. Sci. **141**, 109 (1984).

[115] A. J. Logsdail, D. O. Scanlon, C. R. A. Catlow, and A. A. Sokol, Phys. Rev. B **90**, 155106 (2014).

[116] Y. Kumagai, L. A. Burton, A. Walsh, and F. Oba, Phys. Rev. Appl. **6**, 014009 (2016).

[117] H. M. Evjen, Phys. Rev. **39**, 675 (1932).

[118] S. T. Weir, Y. K. Vohra, and A. L. Ruoff, Phys. Rev. B **33**, 4221 (1986).

[119] K. Momma and F. Izumi, J. Appl. Crystallogr. **44**, 1272 (2011).

[120] *International Union of Crystallography, International Tables of Crystallography A*, 6th ed. (Kluwer, Dordrecht, The Netherlands, 2016).

[121] M. A. Green, Y. Hishikawa, W. Warta, E. D. Dunlop, D. H. Levi, J. Hohl-Ebinger, and A. W. H. Ho-Baillie, Prog. Photovolt. Res. Appl. **25**, 668 (2017).

[122] Y. Hinuma, A. Togo, H. Hayashi, and I. Tanaka, arXiv:1506.01455.

[123] A. Togo, SPGLIB, http://spglib.sourceforge.net/.

[124] I. Semaev, in *Cryptography and Lattices*, edited by J. H. Silverman (Springer, Berlin, 2001), p. 181.

[125] W. Piskorz, J. Gryboś, F. Zasada, S. Cristol, J.-F. Paul, A. Adamski, and Z. Sojka, J. Phys. Chem. C **115**, 24274 (2011).